Particle dynamics in the electron current layer in collisionless magnetic reconnection

Seiji Zenitani[1] and Tsugunobu Nagai[2]
[1)] *Division of Theoretical Astronomy, National Astronomical Observatory of Japan, 2-21-1 Osawa, Mitaka, Tokyo 181-8588, Japan. Electric mail: seiji.zenitani@nao.ac.jp.*
[2)] *Tokyo Institute of Technology, Tokyo 152-8551, Japan*

Particle dynamics in the electron current layer in collisionless magnetic reconnection is investigated by using a particle-in-cell simulation. Electron motion and velocity distribution functions are studied by tracking self-consistent trajectories. New classes of electron orbits are discovered: figure-eight-shaped regular orbits inside the electron jet, noncrossing regular orbits on the jet flanks, noncrossing Speiser orbits, and nongyrotropic electrons in the downstream of the jet termination region. Properties of a super-Alfvénic outflow jet are attributed to an ensemble of electrons traveling through Speiser orbits. Noncrossing orbits are mediated by the polarization electric field near the electron current layer. The noncrossing electrons are found to be non-negligible in number density. The impact of these new orbits to electron mixing, spatial distribution of energetic electrons, and observational signatures, is presented.

arXiv:1605.07472v2 [astro-ph.SR] 18 Aug 2016

I. INTRODUCTION

Collisionless magnetic reconnection is a basic plasma process for the abrupt release of magnetic energy. Understanding the process is crucial to discuss planetary magnetospheres, solar corona, the solar wind, laboratory plasmas, and astrophysical plasma environments. Collisionless reconnection is a highly nonlinear, complex process, in which the electromagnetic field and the plasma particle motion interact with each other. The reconnection mechanism has not yet been fully understood, but numerical simulations provide a way to investigate the underlying physics.

Since early research with particle-in-cell (PIC) simulations, it has been recognized that a small-scale electron-physics layer is embedded inside a broader ion-physics layer in collisionless magnetic reconnection. For example, Pritchett [44] presented a narrowly collimated electron jet inside a broader ion outflow. This picture was further extended by successive PIC simulations,[11,13,17,30,31,50] which were large enough to separate electron-scale structure from the ion-scale structure. Karimabadi et al. [30] and Shay et al. [50] demonstrated that the electron-physics layer evolves into the inner core region and the fast elongated jet. Although these results raised a question concerning long-term behavior of magnetic reconnection,[31] now many scientists agree that the inner core region controls the reconnection rate. The entire layer is often called the electron current layer (ECL) or the electron diffusion layer. Hereafter we call it the electron current layer (ECL).

The inner core is called the dissipation region (DR) or the electron diffusion region (EDR). This is the site of dissipation physics, arising from complex electron motions (See Hesse et al. [24] for a review). As of today, the DR is ambiguously defined, and there are many different opinions on its rigorous definition.[20] Promising signatures to identify the DR are enhanced energy dissipation,[63] electron nongyrotropic behavior,[1,49,57] electron phase-space hole along the inflow direction,[8,26] and characteristic velocity distribution functions (VDFs).[2,40]

The jet is popularly referred to as the super-Alfvénic electron jet, because its bulk speed exceeds the Alfvén speed in the inflow region. This fast jet has characteristic features such as violation of the electron ideal condition,[30,44,50] diamagnetic-type momentum balance,[23] an electron pressure anisotropy,[32] electron nongyrotropy,[1,49,57] bipolar polarization electric fields E_z (the so-called Hall electric fields), and highly structured electron VDFs.[1,2,53] These issues are usually discussed separately. The number of attempts to comprehensively explain these signatures has been limited.

There have been many observational studies on the ECL during magnetic reconnection in the Earth's magnetosphere. Chen et al. [6,7] studied a magnetotail reconnection event with Cluster spacecraft. With the help of a map of electron VDFs by PIC simulation, they identified that the satellite crossed an electron-scale thin current layer near the X-line. Nagai et al. [37] reported an informative reconnection event in the magnetotail with the Geotail spacecraft. They detected both bi-directional electron flows that outrun ion flows and an energy dissipation site around the X-line.[65] Nagai et al. [38] studied another magnetotail reconnection event with ion-electron decoupling. They reported additional signatures in the ion-electron decoupling region, such as the energetic electron fluxes. Oka et al. [41] reported a DR-crossing in the magnetotail with THEMIS. They observed nongyrotropic electron VDFs and perpendicular heating inside the ECL. They also showed that the ECL is a site of electron energetization. In addition, there have been several observations of super-Alfvénic electron jets inside the reconnection outflow exhaust in the magnetosheath,[42] in the magnetotail,[68] and in the solar wind.[61] These results support the standard picture of the ECL, the central DR and extended electron jets.

In the above observations, time and spatial resolutions were rather limited to discuss electron physics in great detail. In order to probe electron-scale structures in near-Earth reconnection sites at ultra-high resolutions,

NASA recently launched the Magnetospheric MultiScale (MMS) spacecraft in 2015.[4] MMS is planned to move to the Earth's magnetotail in 2017, where magnetic reconnection often occurs in an anti-parallel configuration. It is expected that MMS will encounter ≈10 reconnection events.[19] Once it encounters reconnection events, MMS is expected to resolve the aforementioned structures.

Since spacecraft observe VDFs, it is important to understand the electron motion behind the VDFs in PIC simulations. Hoshino et al.[28] was one of the first to discuss electron VDF and associated particle motion. They examined VDFs near the magnetic island in the downstream region. Egedal et al.[15,16] found that electron VDFs are elongated in the field-aligned direction in the inflow region. As already introduced, Chen et al.[6,7] studied spatial distribution of electron VDFs by PIC simulation to interpret satellite data.

In order to prepare for the MMS observation, a growing number of works are devoted to electron VDFs in PIC simulations. Ng et al.[40] visualized the complex structure of the electron VDF in the DR. They reconstruct the VDF at high resolution, by back-tracing particle orbits in the PIC field and by using a Liouville's theorem. The VDF contains discrete striations in a triangular-shaped envelope. Shuster et al.[52,53] presented that electron VDFs contain various discrete components in the outflow exhaust. They further examined the structure of the electron VDF over the ECL, with help from test-particle simulations. Bessho et al.[2] examined electron VDFs in the ECL. In the DR, they gave semi-analytic expressions to the fine structure of the VDF. In the downstream, many arcs were found in the VDFs and they were attributed to a gradual remagnetization of electrons. Cheng et al.[10] inferred particle dynamics in driven reconnection from the spatial distribution of VDFs. They claimed that the field-aligned electron population in the inflow region is injected into the super-Alfvénic electron jet. Most recently, Wang et al.[59] studied the electron heating mechanism in the exhaust region in detail. With help from test particle simulations, they found that parallel heating by the curvature drift acceleration and perpendicular heating by the gradient-B drift acceleration account for a highly structured VDF near the magnetic flux pile-up region.

These VDFs are ensembles of electrons, following various complex trajectories in the reconnection system. In addition to a gyration and a parallel motion, several classes of electron particle motions are reported in the previous literature, such as a Speiser motion around the DR[2,40,55] and a field-aligned bounce motion in the inflow region.[15,16] They are proven to be building blocks of the VDFs. However, it is not clear whether these particle motions and/or their combinations can explain everything about electron VDFs. In fact, as reviewed in this section, the ECL structure is found to be much more complicated than previously expected. It is possible that some electrons travel through new orbits near the reconnection site and that they have an impact on the reconnection dynamics and observational signatures. In order to better interpret the electron VDFs to deeper discuss kinetic reconnection physics, it is important to understand electrons particle orbits and dynamics in a modern reconnection simulation.

The purpose of this paper is to comprehensively discuss electron fluid properties, VDFs, self-consistent trajectories, and relevant particle dynamics around the ECL in magnetic reconnection. The paper is organized as follows. First, we briefly review nongyrotropic particle motions in a curved magnetic field in Section II. Next, we describe the numerical setup of a 2D PIC simulation in Section III. The simulation results are presented in several ways. Section IV presents macroscopic fluid quantities. In Section V, we present electron kinetic signatures such as VDFs and phase-space diagrams. In Section VI, we will discuss self-consistent electron trajectories in detail. In Section VII, we utilize the trajectory datasets to further examine VDFs and spatial distribution of electrons. The relevance to the satellite observation is briefly addressed in Section VIII. Section IX contains discussions and summary.

II. ELECTRON MOTION IN A CURVED FIELD REVERSAL

We outline basic properties of particle (electron) trajectories in a highly bent magnetic field.[3,5] Here we consider a simple parabolic field,

$$\boldsymbol{B} = B_0(z/L)\boldsymbol{e}_x + B_n\boldsymbol{e}_z, \quad \boldsymbol{E} = 0, \tag{1}$$

where B_0 is the reference magnetic field, L is the length scale of the current sheet, and B_n is the normal magnetic field. This system resembles the outflow region in magnetic reconnection at the lowest order. The equation of motion, $m_e(d\boldsymbol{v}_e/dt) = -e(\boldsymbol{v}_e \times \boldsymbol{B})$, can be rewritten

$$\begin{cases} \ddot{x} = & -\Omega_n\dot{y} & (2a) \\ \ddot{y} = & -\omega_b^2(\dot{z}/|v_e|)z + \Omega_n\dot{x} & (2b) \\ \ddot{z} = & \omega_b^2(\dot{y}/|v_e|)z & (2c) \end{cases}$$

where $\Omega_n = eB_n/m_e$ is the gyrofrequency about B_n and $\omega_b = \sqrt{eB_0|v_e|/m_eL}$ is a characteristic frequency. The electron motion is characterized by the ratio of the two frequencies,[3]

$$\kappa \equiv \frac{\Omega_n}{\omega_b} = \sqrt{\frac{R_{\mathrm{c,min}}}{r_{\mathrm{L,max}}}} = \left|\frac{B_n}{B_0}\right|\sqrt{\frac{L}{r_{\mathrm{L,max}}}}, \tag{3}$$

where $R_{\mathrm{c,min}}$ is the minimum curvature radius of magnetic field line and $r_{\mathrm{L,max}} = m_e|v_e|/eB_n$ is the electron's maximum gyroradius. This parameter is known as the curvature parameter. The curvature radius solely depends on the field-line geometry, while the gyroradius $r_{\mathrm{L,max}}$ depends on the electron velocity $|v_e|$ or the electron energy $\mathcal{E} \equiv \frac{1}{2}m_ev_e^2$. Note that both $|v_e|$ and $\mathcal{E}$ are constant in this system, because $\boldsymbol{E} = 0$.

When $\kappa \gg 1$, the gyration about B_n dominates. If the parameter falls below the unity, $\kappa \lesssim 1$, the electron motion becomes nongyrotropic. In particular, the motion becomes highly chaotic for $\kappa \sim 1$ ($\Omega_n \sim \omega_b$), because the two oscillations of different kinds interfere with each other. Several characteristic orbits appear for $\kappa \ll 1$, as will be shown in the next paragraphs.

Figure 1 demonstrates typical electron orbits for $\kappa = 0.1$ in the 3D space (Fig. 1a), the velocity space (Figs. 1b and 1c), and the phase-space (v_z–z; Fig. 1d). Parameters are chosen to be $|R_c| = 1$ and $|v_e| = 1$. The blue orbit demonstrates a well-known Speiser orbit.[55] After entering the midplane from the upper left, it slowly turns its direction from $-x$ to $+x$ due to the gyration about B_n. Then it exits in the $+x$ direction. Near the midplane ($z \sim 0$), the electron mainly travels in $-y$, while bouncing in z at the frequency of ω_b ($\dot{y} \approx -|v_e|$ in Eq. (2c)). This is the so-called meandering motion. In the velocity space, the B_n-gyration near the midplane corresponds to a half circle in v_x–v_y, as can be seen in Figure 1c. The electron velocity rotates anti-clockwise from $-v_x$ to $+v_x$. The fast z-bounce motion is evident in $\pm v_z$, as indicated by the arrow in Figure 1b. Since the meandering motion consists of two opposite gyrations, the electron moves back-and-forth along arcs in $\pm v_z$. It finally exhibits a zigzag pattern in the 3D velocity space. The z-bounce motion also corresponds to the rotation around the center in the phase-space (Fig. 1d).

The red orbit belongs to another kind of nongyrotropic orbit. It is called a regular orbit or an integrable orbit.[5] When the z-motion fully resonates with the gyration about B_n, the electron travels through a figure-eight-shaped orbit, hitting a fixed point at the midplane (See also the left panel of Fig. 4 in Ref. 5). In the vicinity of the figure-eight-shaped orbit, electrons keep bouncing in z and do not escape away from the midplane. It was further shown that the electrons are trapped on the surface of a ring-type torus, but the reader is referred to Büchner & Zelenyi[3] paper for detail. Because of the z-bounce motion, we usually see closed circuits in the phase space (Fig. 1d). Note that the regular-orbit electrons travel in $+v_y$ near the midplane ($z \sim 0$). They appear in the $+v_y$ side in the velocity space near the midplane (Fig. 1c).

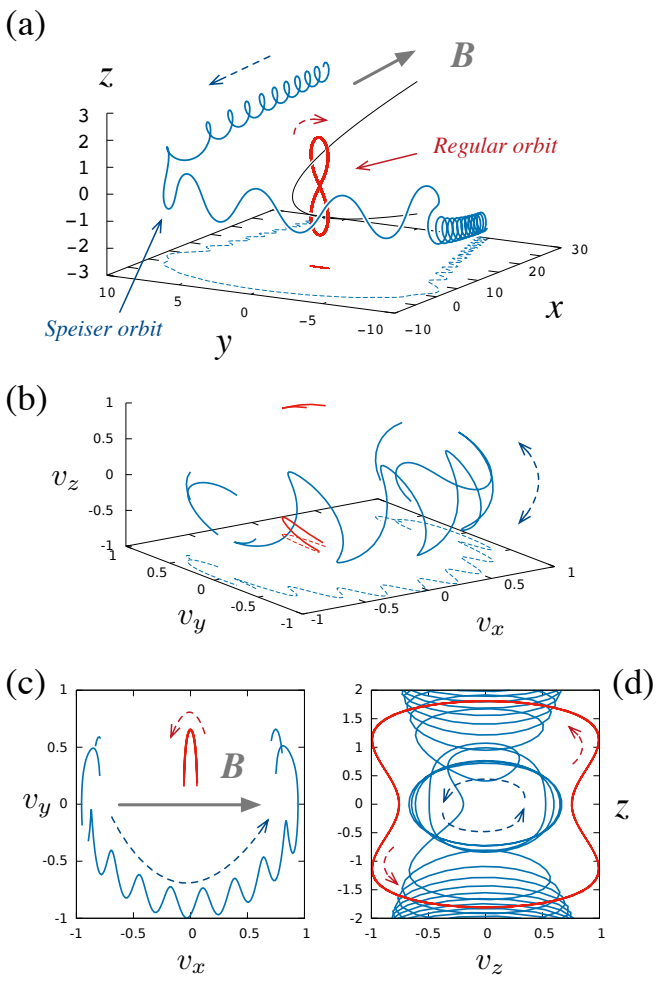

FIG. 1. (Color online) (a) Nongyrotropic electron orbits in a curved field reversal for $\kappa = 0.1$. A Speiser orbit (blue) and a regular orbit (red). (b) 3D velocity-space orbits of the electrons near the midplane $|z| < 1$. (c) 2D velocity-space orbits in the v_x–v_y plane. (d) Phase-space diagram for the Speiser and regular orbits in v_z–z.

III. SIMULATION

We use a partially implicit PIC code[22] to study our reconnection problem. The length, time, and velocity are normalized by the ion inertial length $d_i = c/\omega_{pi}$, the ion cyclotron time $\Omega_{ci}^{-1} = m_i/(eB_0)$, and the ion Alfvén speed $c_{Ai} = B_0/(\mu_0 m_i n_0)^{1/2}$, respectively. Here, $\omega_{pi} = (e^2 n_0/\varepsilon_0 m_i)^{1/2}$ is the ion plasma frequency, and n_0 is the reference density. We employ a Harris-like configuration, $\boldsymbol{B}(z) = B_0 \tanh(z/L)\hat{\boldsymbol{x}}$ and $n(z) = n_0 \cosh^{-2}(z/L) + n_b$, where the half thickness is set to $L = 0.5d_i$ and $n_b = 0.2n_0$ is the background density. The ion-electron temperature ratio is $T_i/T_e = 5$. The mass ratio is $m_i/m_e = 100$. The ratio of the electron plasma frequency to the electron cyclotron frequency is $\omega_{pe}/\Omega_{ce} = 4$. Our domain size is $x, z \in [0, 76.8] \times [-19.2, 19.2]$. It is resolved by 2400×1600 grid cells. Periodic (x) and reflecting wall (z) boundaries are employed. 1.7×10^9 particles are used. Reconnection is triggered by a small flux perturbation, $\delta A_y = -2LB_1 \exp[-(x^2 + z^2)/(2L)^2]$, where $B_1 = 0.1B_0$ is the typical amplitude of the perturbed fields. The initial electric current is configured accordingly.

This run was analyzed in our previous paper on ion VDFs and ion particle dynamics.[66] The parameters and system evolution are similar to those in run 1A in Ref. 64 on the electron-scale structure. Several aspects of this reconnection system were presented in these papers. We explore new aspects of electron VDFs and particle dynamics in this paper.

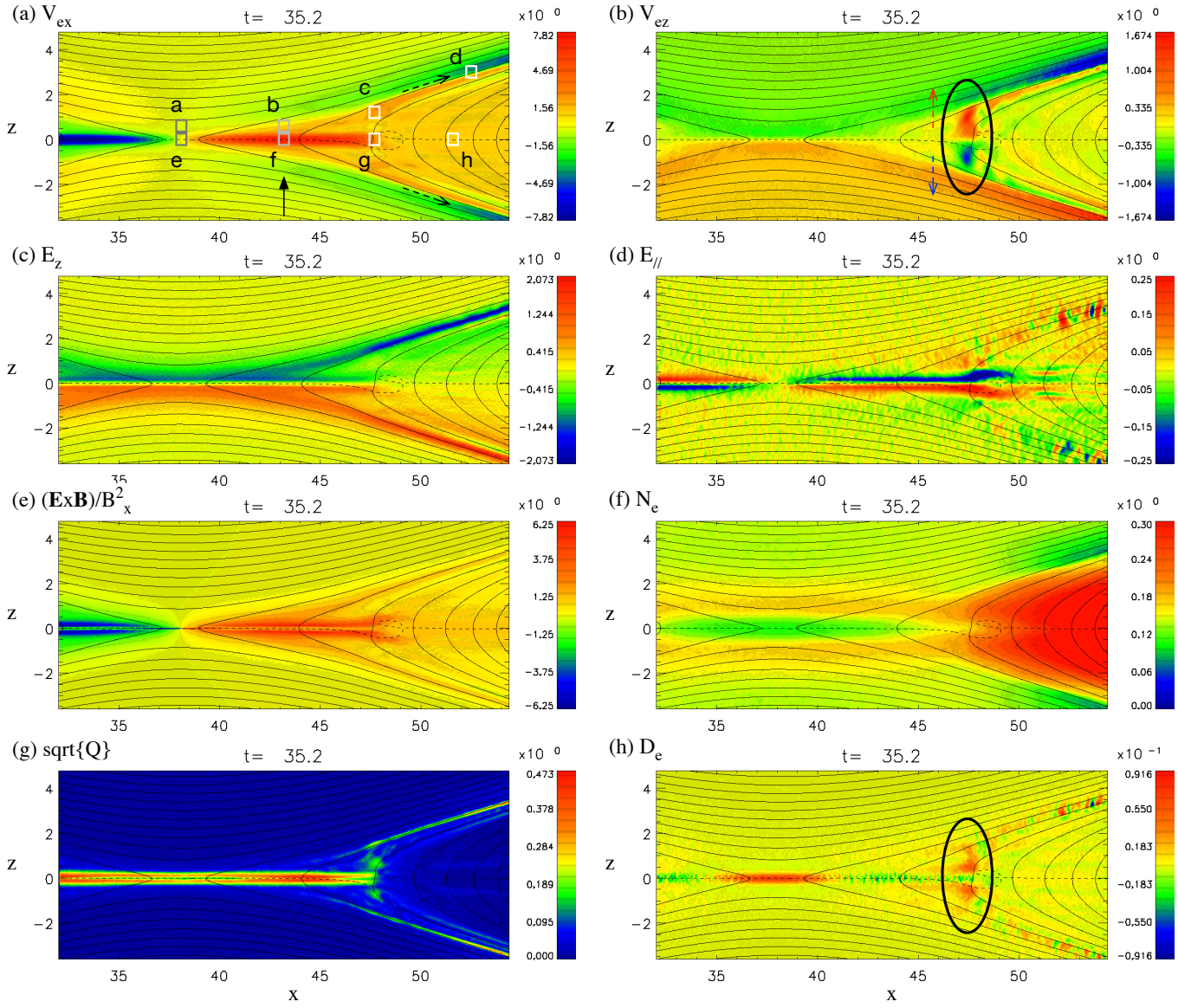

FIG. 2. (Color online) Results of the main run, averaged over $t = 35$–35.25. The contour lines are in-plane magnetic field lines and the dashed line indicates the field reversal, $B_x = 0$. (a) The electron outflow speed V_{ex} in a unit of c_{Ai}, (b) the vertical electron flow V_{ez}, (c) the vertical electric field E_z in a unit of $c_{Ai}B_0$, (d) the parallel electric field $E_\parallel$, (e) the $\mathbf{E}\times\mathbf{B}$ outflow speed w_x, (f) the electron density n_e, (g) the nongyrotropy measure $\sqrt{Q}$, and (h) the nonideal energy dissipation $\mathcal{D}_e$.

IV. FLUID QUANTITIES

The reconnection occurs at the center of the simulation domain. The magnetic flux transfer rate across the X-line grows in time until $t \approx 14.5$. If normalized by quantities at $3d_i$ upstream of the X-line, the reconnection rate reaches 0.14, gradually decreases to 0.11 at $t \approx 25$, and then remains constant after that. An electron jet as well as other electron-scale structures grows in time. They are well developed at the time of our interest, $t = 35$. We study this time step, because we studied other aspects in our previous studies,[64,66] and because it is early enough to avoid major effects from the periodic boundary in x. In fact, the electron jet continues to evolve until $t \approx 44$,[64] but minor boundary effects appear in particle signatures at $t \approx 35$, as will be shown later.

Figure 2 shows various fluid and field quantities of our PIC simulation at $t = 35$. They are averaged over $\Delta t = 0.25$ to remove noises. The X-line is located at $(x, z) = (38.1, 0.0)$. Figure 2a shows the x component of the electron bulk velocity $\boldsymbol{V}_e$. One can see narrow bi-directional electron jets from the X-line. The rightward jet ranges $38.1 < x < 48$. The jet speed is higher than the ion bulk speed V_{ix} and the inflow Alfvén speed ≈ 1.62 at this time. This is consistent with previous studies.[30,44,50] It has been known that electrons are unmagnetized in the

electron jet region, while they are magnetized again farther downstream. Ref. 64 called the jet front boundary ($x \approx 48$) an "electron shock," but it would be more appropriate to call it the "remagnetization front." In the downstream of the remagnetization front, unmagnetized ions form a broad current layer.[34,66] Properties of this ion current layer was studied in our previous work.[66] In Figure 2b, it is interesting to see electron divergent flows in the vertical ($\pm z$) directions near the remagnetization front. The maximum jet speed is $|V_{ez}| = 1.67$, also comparable with the inflow Alfvén speed. These divergent flows generate the vertical electric currents J_z, which correspond to a step-shaped pattern in the out-of-plane magnetic field B_y (See Figs. 1c and 3 in Ref. 66). Obviously the super-Alfvénic electron jet is responsible for the divergent flows. These electron flows further correspond to narrow electron jets in red ($V_{ex} > 0$) near the separatrices at $x > 47$, as the dashed arrows indicate in Figure 2a. These jets penetrate into a broader distribution of incoming electrons ($V_{ex} < 0$). Hereafter we call these jets the "field-aligned electron outflows." Similar electron jets were reported by recent studies.[66,67]

Figure 2c shows the vertical electric fields E_z. They consist of a large-scale X-shaped structure along the separatrices and a small-scale bipolar structure along the electron jet region. They are polarization electric fields, due to a broad ion distribution and a narrow electron distribution. Figure 2d shows the parallel electric field $E_\parallel$. To better see a weak background structure, we smooth it with boxcar averaging over ∼0.16 and then we adjust the range of the color bar. Aside from plasma instabilities along the separatrices, one can recognize a double quadrupole structure.[7,45] The first inner quadrupole is found near the midplane. It features a strong $E_\parallel$ toward the X-line, a projection of the Hall electric field E_z. This inner quadrupole plays a crucial role for electron dynamics, as will be shown in Section VI B. The second outer quadrupole features the parallel field $E_\parallel$ away from the X-line. Although they are hard to recognize, one can see $E_\parallel > 0$ in the first quadrant ($x \gtrsim 45, z > 0$) and $E_\parallel < 0$ in the lower half ($x \gtrsim 45, z < 0$) inside the exhaust region. The other two quadrants are found outside the displayed domain ($x \lesssim 31$). This quadrupole is a projection of the reconnection electric field E_y to the quadrupole Hall magnetic field B_y.[54] The incoming electrons near the separatrices, discussed in the previous paragraph, are weakly accelerated toward the X-line by this $E_\parallel$.

Figure 2e shows the x component of the ideal flow vector, $\boldsymbol{w} \equiv \boldsymbol{E} \times \boldsymbol{B}/B^2$. Although it saturates in the close vicinity of the X-line ($37 \lesssim x \lesssim 39, z \approx 0$), it exhibits a characteristic picture. It looks bifurcated in the electron jet region: It is super-Alfvénic $w_x = 5$–6 on the upper and lower sides of the electron jet. Strangely, it is relatively low $w_x = 2$–3 at the midplane $z = 0$. It is also enhanced along the separatrices. These structures are largely attributed to the Hall electric field E_z (Fig. 2c). We also note that w_y looks bifurcated in the electron jet region [not shown].

Figure 2f shows the electron density n_e. The ion density looks similar [not shown]. We adjust the color bar $0 < n_e < 0.3$ for discussion later in this paper, while the density reaches $n_e = 0.37$ in the downstream side. At this stage, the reconnection process has flushed out the Harris current sheet into the outflow region. The reconnection region is occupied by the inflow plasmas, whose initial density is $n_b = 0.2$. The typical electron density is $n_e \sim 0.1$–0.2 around the center. One can see two high-density yellow bands around $30 < x < 45$. This consists of a plasma distribution over an ion meandering width ($|z| < 2$–3) and a density cavity near the midplane ($|z| < 1$) in green. The cavity stretches in x and it covers the electron jet region.

Figure 2g displays a nongyrotropy measure $\sqrt{Q}$, which quantifies the deviation of the electron VDF from gyrotropic one.[57] It is defined in the following way,

$$\sqrt{Q} \equiv \left\{ \frac{P_{e12}^2 + P_{e13}^2 + P_{e23}^2}{P_{e\perp}^2 + 2P_{e\perp}P_{e\parallel}} \right\}^{1/2}, \tag{4}$$

where $\overleftrightarrow{P}_e$ is the electron pressure tensor. The subscripts ($\parallel, \perp$) and numeral subscripts indicate the parallel, perpendicular, and three off-diagonal components of $\overleftrightarrow{P}_e$ in the field-aligned coordinates. Equation (4) ranges from 0 in the fully gyrotropic case to 1 in the nongyrotropic limit. In Figure 2g, the measure highlights the ECL near the midplane. If one takes a closer look, two narrow bands are highlighted along the electron jets. These are consistent with previous studies.[1,49,53] It also marks small-scale regions near the remagnetization front and the separatrices farther downstream $x > 47$.

Figure 2h shows a frame-independent energy dissipation, $\mathcal{D}_e = \gamma_e[\boldsymbol{J} \cdot (\boldsymbol{E} + \boldsymbol{V}_e \times \boldsymbol{B}) - \rho_c(\boldsymbol{V}_e \cdot \boldsymbol{E})]$, where $\gamma_e = [1 - (V_e/c)^2]^{-1/2}$ is the Lorentz factor and ρ_c is the charge density.[63] This is equivalent to the nonideal energy conversion in the nonrelativistic MHD in a neutral plasma. The measure marks the electron-scale dissipation region around the X-line. In addition, it also marks the vertical flow region, as indicated by the circle.

Let us take a closer look at the electron jet. Panels in Figure 3 show 1D cuts at $x = 43.2$. The black arrow in Figure 2a indicates this x-position. The velocity profile (Fig. 3a) tells us that the electron perpendicular flow outruns the ideal MHD velocity ($V_{e\perp x} \approx V_{ex} > w_x$) around the ECL ($|z| < 0.2$) and that the electron are threaded by the magnetic field ($\boldsymbol{V}_{e\perp} \simeq \boldsymbol{w}$) outside the ECL. The profile of w_x is bifurcated, as discussed in the previous section. The bifurcation of w_x can be seen in Figure 2 in Hesse et al.[23] as well. The y components ($V_{e\perp y}$ and w_y) are similarly bifurcated and $V_{e\perp y}$ outruns w_y in the $-y$ direction near the midplane. We note that $V_{ex} < V_{e\perp x}$ and $V_{ey} < V_{e\perp y}$ outside the ECL, because there is a field-aligned electron outflow in the $(-x, +y)$ direction toward the X-line.

Figure 3b displays the variation in the field properties. Both the reconnecting magnetic field B_x and the

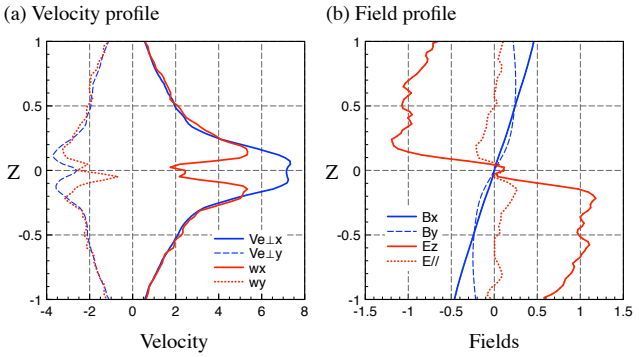

FIG. 3. (Color online) 1D profiles across the electron jet at $x = 43.2$, averaged over $t = 35$–35.25. (a) The electron perpendicular flow $\boldsymbol{V}_{e\perp}$ and the ideal flow $\boldsymbol{w}$. (b) The field properties. The electric field is normalized by $c_{Ai}B_0$.

Hall magnetic field B_y change their polarities across the midplane. The Hall electric field E_z has a large-scale bipolar structure. It is negative in $z > 0$ and positive in $z < 0$. Its amplitude is eight times stronger than the reconnection electric field $|E_y| = 0.15$. This also corresponds to the bipolar $E_\parallel$ at $|z| \lesssim 0.5$. Note that parallel electric field remains nonzero in any moving frame, because $\boldsymbol{E}\cdot\boldsymbol{B}$ is invariant. Outside there, since $E_\parallel \simeq 0$ and since $\boldsymbol{V}_{e\perp} \simeq \boldsymbol{w}$, the electron ideal condition is recovered, $\boldsymbol{E} + \boldsymbol{V}_e \times \boldsymbol{B} \simeq 0$. In a close vicinity of the midplane, $|z| < 0.1$, one can recognize a reverse bipolar structure in E_z and $E_\parallel$. It is positive in $z > 0$ and negative in $z < 0$. This is an electrostatic field due to the electron meandering motion in z.[8]

V. KINETIC SIGNATURES

Panels in Figure 4 show electron velocity distribution functions (VDFs) at various locations at $t = 35$. These VDFs are computed in small boxes of 0.5×0.5. The boxes are indicated in Figure 2a and the figure titles indicate the box center positions. The VDFs are two-dimensional. The electron number is integrated in the third direction.

The top four panels (Figs. 4a–d) display VDFs (v_x–v_z) around the upper boundary regions. Note that we use lowercase $\boldsymbol{v}$ for the particle velocity in order to distinguish it from the bulk velocity $\boldsymbol{V}$. Figure 4a shows the electron VDF in v_x–v_z just above the X-line. It looks highly anisotropic. Here, the magnetic field is directed in x, and so the electrons are heated in the parallel direction. Egedal et al.[15,16] explained that the electrons are trapped by the parallel potential and that they are fast traveling in the field-aligned directions. Figure 4b is a VDF at $(x, z) = (43.2, 0.6)$. It looks slightly tilted, because the magnetic field is directed in a slightly upward direction. These two VDFs are gyrotropic. The nongyrotropy measure does not mark these regions (Fig. 2g).

The third panel (Fig. 4c) shows a VDF at $(x, z) = (47.7, 1.2)$. In addition to the field-aligned component, one can see a hot outgoing component in the right half. A similar VDF was reported by Chen et al.[6] (#10 in Fig. 4; §2.2.2 in Ref. 6). The hot component looks partially gyrotropic; the electrons are found in the $v_{ey} < 0$ half in v_y [not shown]. As a result, the entire VDF is weakly nongyrotropic, because two or more components start to mix with each other here. The $\sqrt{Q}$ measure weakly marks this and nearby regions (Fig. 2g). Interestingly, this hot component suddenly appears here. We do not find it in the separatrix regions closer to the X-line. In Figure 4d, one can see two field-aligned components, a cold incoming component and a high-energy outgoing component. The cold electrons are weakly accelerated by $E_\parallel$ toward the X-line. We will discuss the outgoing electrons later in this paper. Since both populations are gyrotropic, the VDF is anistropic but gyrotropic.

Panels in the bottom three rows show VDFs at four locations at the midplane. The VDFs in v_x–v_y (the second row), in v_x–v_z (the third), and in v_y–v_z (the bottom row) are presented. Figure 4e exhibits typical signatures of a VDF in the DR. Compared with the inflow region (Fig. 4a), the VDF is stretched in $-y$, due to the y acceleration by the reconnection electric field E_y. The VDF in v_x–v_y looks triangular.[2,40,53] Small v_x electrons stay longer in the DR and therefore they are more accelerated in $-y$.[47] The structure in v_z is not so clear, because our box size in z ($\Delta z = 0.5$) is larger than the electron meandering width. The electron VDFs in $|z| < 0.1$ are bifurcated in v_z [not shown], as reported by previous studies.

Figure 4f shows the VDF at $(x, z) = (43.2, 0)$ in the middle of the electron jet. The overall VDF is shifted in $+v_x$ in agreement with the fast bulk flow. The bulk velocity is $\boldsymbol{V}_e \approx (+7, -3, 0)$. The electrons are spread in v_x–v_y, while they are confined in v_z. At the midplane $z = 0$, the magnetic field is directed in z and so the electron perpendicular pressure exceeds the parallel pressure. This VDF is highly nongyrotropic $\sqrt{Q} \approx 0.4$, as evident in Figure 2g. In v_x–v_y (Fig. 4f1), one can see a narrow ridge in the right, as indicated by the white arrow. This is related to y-accelerated electrons in the DR, indicated the white arrow in Figure 4e1. As we depart from the X-line, the bottom ridge in Figure 4e1 rotates anticlockwise and then evolves into the right ridge in Figure 4f1. In v_y–v_z (Fig. 4f3), the VDF is weakly bifurcated in v_z for $v_{ey} < 0$.

Figure 4g shows the VDF at $(x, z) = (47.7, 0)$ in the jet termination region. The VDF looks fairly isotropic in v_x–v_y. In the bottom two panels, the major outgoing component looks similar to one in Figure 4f. In addition, one can recognize a hot low-density component in the $v_x < 0$ half. These electrons come from the downstream region and then they start to spread in $\pm v_z$. This corresponds to the vertical divergent flows in Figure 2b.

Figure 4h shows the VDF at $x = 51.6$, downstream of the remagnetization front. The electrons are isotropic in all three planes. One can recognize two small peaks in v_y–v_z, as indicated by the arrows in Panel h3. Sim-

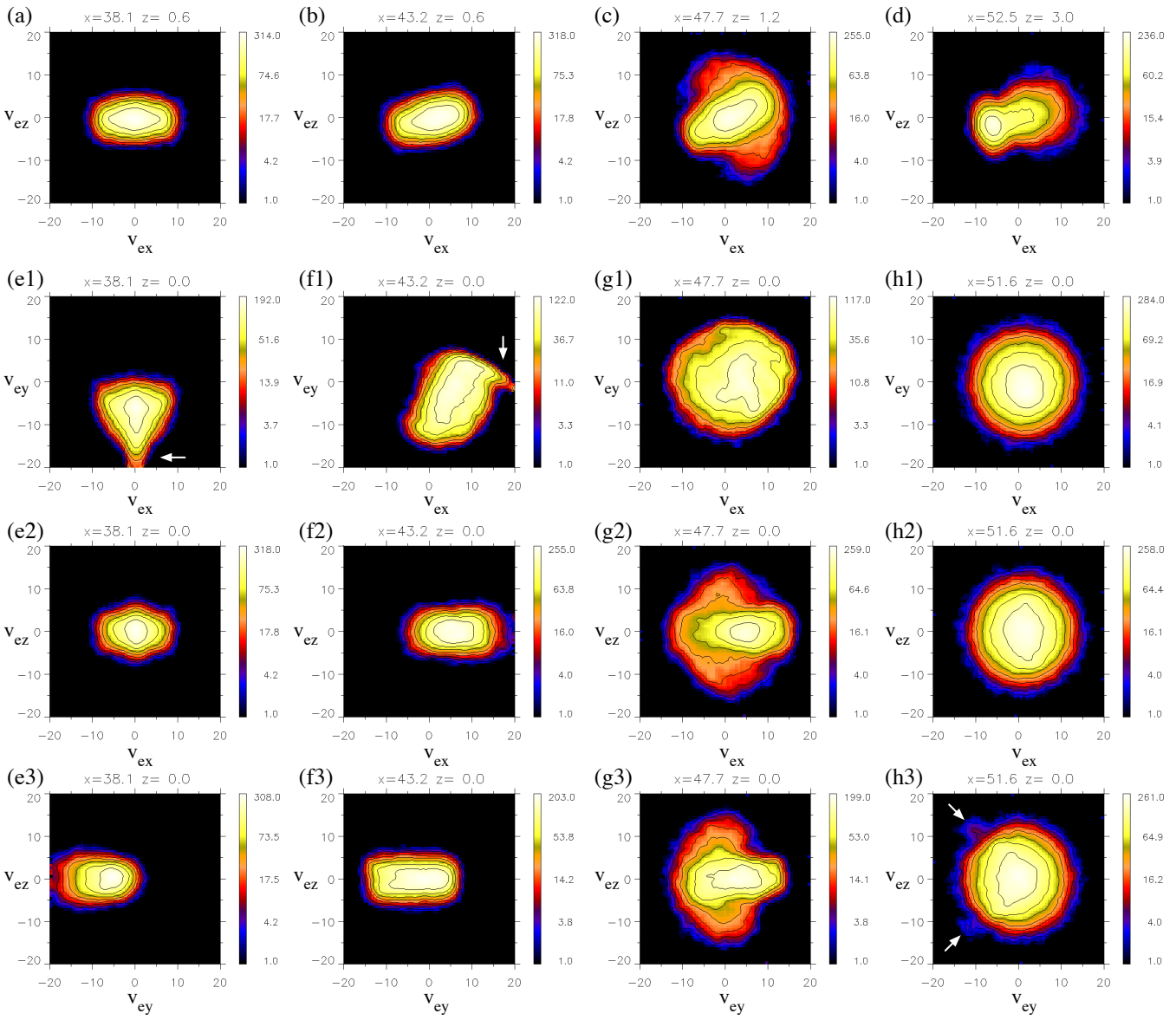

FIG. 4. (Color online) Electron velocity distribution functions (VDFs) at $t = 35$. They are computed in a box size of 0.5×0.5. The box positions are indicated in Figure 2a. For (a-d), one VDF (v_x–v_z) is presented. For (e-h), all three VDFs are presented. Electron numbers are integrated in the third (out-of-plane) dimension.

ilar components in VDFs were reported by Shuster et al. [52]. These energetic electrons travel backward from the downstream magnetic island, but it is not clear how they are accelerated. This is one of the earliest signals from the downstream region. To avoid side-effects from the downstream, we limit our attention to the upstream side, $x \lesssim 51.6$.

Figure 5 provides additional information to electron kinetic physics. Figure 5a shows the phase-space diagram in v_y–z along the inflow line at $x = 38.1$. Here, as the electrons travel in $\pm z$ from the inflow regions toward the midplane $z = 0$, they start to drift in $-y$ due to the polarization electric field E_z. Once they enter the ECL, they are accelerated by the reconnection electric field E_y through Speiser motion.[55] In the v_z–z diagram (Fig. 5b), a circle around the central hole corresponds to a bounce motion during the Speiser motion.[8,26] Interestingly, the electron density is high outside the ECL, $|z| \gtrsim 0.5$ (Figs. 5a and 5b). Figure 5c is the energy-space diagram in $\mathcal{E}$–z, where $\mathcal{E} = \frac{1}{2} m_e v_e^2$ is the electron kinetic energy, normalized by $m_i c_{Ai}^2$. High-energy electrons ($\mathcal{E} > 1.0$) are only found inside the ECL, $|z| < 0.25$.

The right Panels show similar diagrams for the electron jet region at $x = 43.2$. Figures 5d and 5e are the v_x–z and v_z–z diagrams. The electrons are accelerated in x (Fig. 5d) and one can see a phase-space hole in Figure 5e. There are high-density regions outside the ECL, $|z| \gtrsim 0.5$ (Figs. 5d and 5e). In Figure 5f, although medium-energy

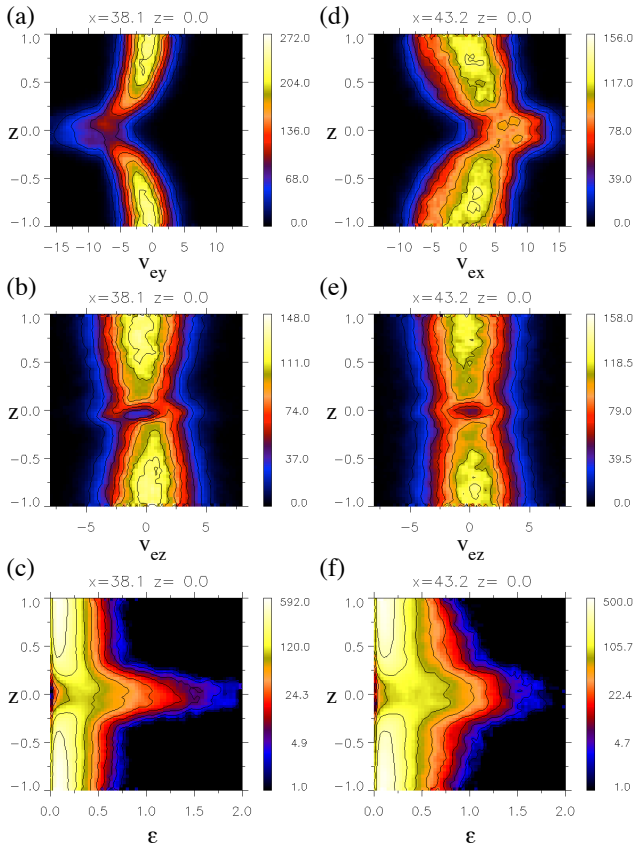

FIG. 5. (Color online) Phase-space and energy-space distributions at $t = 35$. The left panels are (a) the v_y–z distribution, (b) the v_z–z distribution, and (c) the $\mathcal{E}$–z distribution across the X-line ($x = 38.1$). The right panels are (d) the v_x–z distribution, (e) the v_z–z distribution, and (f) the $\mathcal{E}$–z distribution across the electron jet region ($x = 43.2$).

electrons ($\mathcal{E} = 0.5$–1.0) are distributed wider in z, high-energy electrons ($\mathcal{E} > 1.0$) are confined around the ECL.

VI. PARTICLE TRAJECTORIES

In this work, we manage to record as many electron trajectories as possible in our PIC simulation. Using the particle ID number, we select 3% (1/32) of electrons without bias. Then we output the selected particle data to a hard drive every two plasma periods $\Delta t = 2\omega_{pe}^{-1}$ during $30 < t < 36.25$. The time interval is comparable with one ion gyroperiod, $6.25 \approx 2\pi$. The time resolution is sufficient to see electron gyrations, i.e., the typical electron gyroperiod is $2\pi\Omega_{ce}^{-1} \approx 25\omega_{pe}^{-1} \gg \Delta t$. It is even sufficient for plasma oscillations around the reconnection site, i.e., $2\pi\omega_{pe}^{-1}(n_b/n_0)^{-1/2} \approx 14\omega_{pe}^{-1} > \Delta t$. As a result, we obtain 2.3×10^7 electron trajectories. We introduce characteristic trajectories in our dataset in the following subsections.

A. Speiser orbits

Panels in Figure 6 show the first set of representative trajectories. The electron orbits during the interval are presented in spatial/energy/velocity/phase spaces. The circles indicate their positions at $t = 35$. The first orbit in red is a typical Speiser orbit.[55] In the x–z space (Fig. 6a), this electron comes from the bottom left to enter the DR. Then it is accelerated in the $-y$ direction by the reconnection electric field E_y (Fig. 6b). As a consequence, it quickly gains energy near the X-line (Fig. 6c). The electron gradually turns in the $+x$ direction (Fig. 6b), while staying around the midplane ($z \approx 0$; Fig. 6a). Finally it escapes from the midplane to the upper right, gyrating about the magnetic field line. In the v_x–v_y space (Fig. 6d), it initially starts from the center, moves downward in $-v_y$ due to the y-acceleration near the X-line, rotates anti-clockwise as it turns in v_x, and then exhibits larger gyration after it exits from the midplane. The z-bounce motion around the midplane is also evident in the central circles in the v_z–z space (Fig. 6g).

The second orbit in green is another example of the Speiser orbit. This one is much more accelerated around the X-line than the first one (Fig. 6c). After the Speiser rotation, this electron wanders around the midplane, $|z| \lesssim 1$, in the downstream region ($x \gtrsim 47$). This is interesting, because we expect that the electron escapes along the field line like in the first orbit after the Speiser motion.

The third orbit in blue represents a Speiser motion of different kind. The electron comes from the upper right and reaches the midplane at $x \approx 43$ (Fig. 6a). There, it slowly gyrates about B_z, turns its direction from $-y$ to $+x$ while bouncing in z. Instead of passing through the DR, it is locally reflected to the downstream. This is a Speiser orbit of local reflection-type. Following our previous work on ion orbits,[66] we call this blue electron orbit a "local Speiser orbit," and the previous red and green orbits "global Speiser orbits." The blue electron gains less energy than the other electrons through global Speiser orbits. This is because the local magnetic field B_z is stronger, and because the electron turns more quickly than in the DR. During the local reflection phase, the velocity vector rotates anti-clockwise from $-v_y$ to $+v_y$ (Fig. 6d). This is because the magnetic field line also turns from $\pm x$ near the X-line to $\pm y$ near $x \approx 47$, where this blue electron escapes from the midplane. Interestingly, the electron still remains near the midplane, $|z| \lesssim 1$, chaotically bouncing in z, similar to the second electron in green.

Let us examine the first and third orbits near $x = 43.2$ in more detail. Both are located near the midplane ($|z| \lesssim 0.1$; Figs. 6a, 6f, and 6g) at $t = 35$. In such close vicinity to the midplane, both B_x and B_y are approximately linear in z (Fig. 3b), while B_z is roughly constant, $B_z \approx 0.06$. This configuration is similar to the system in Section II, (1) if the system is uniform in x and (2) if we switch to an appropriately moving frame

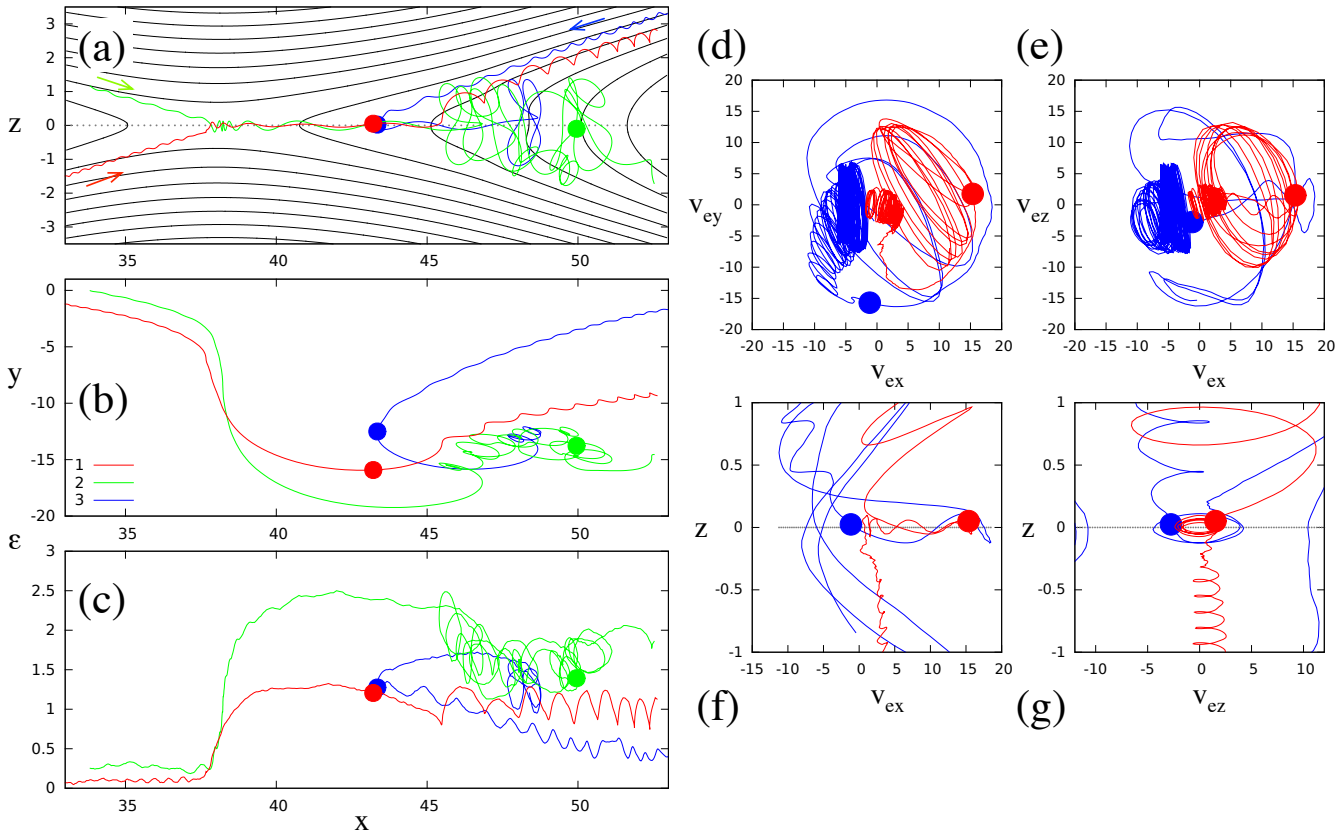

FIG. 6. (Color online) Selected electron orbits during $30 < t < 36.5$ in spatial/energy/velocity/phase spaces: (a) x–z plane, (b) x–y plane, (c) x–$\mathcal{E}$ space, (d) v_x–v_y velocity space, (e) v_x–v_z velocity space, (f) v_x–z phase space, and (g) v_z–z phase space. The right panels focus on the first (red) and the third (blue) electrons. The circles indicate the particle positions at $t = 35$. The energy $\mathcal{E}$ is normalized by $m_i c_{Ai}^2 = m_e(10c_{Ai})^2$ in (c).

in which the electric field vanishes. Even though the two conditions are not exactly met in the PIC simulation, the theory provides insight into electron motions. We fit the magnetic field across the midplane at $x = 43.2$ to the parabolic model (Eq. (1)) to obtain the magnetic curvature radius $R_{\rm c,min}$. A similar procedure is presented in Section III B in Ref. 66. At $x = 43.2$, the field line is so sharply bent that the curvature radius is $R_{\rm c,min} = 0.068$. The electron maximum Larmor radius and the curvature parameter are as follows,

$$\frac{r_{\rm L,max}}{d_i} = \Big(\frac{v_e'}{c_{Ai}}\Big)\Big(\frac{m_e}{m_i}\Big)\Big(\frac{B_0}{|B_z|}\Big) \approx 1.64\Big(\frac{v_e'}{10c_{Ai}}\Big) \qquad (5)$$

$$\kappa \approx 0.2\Big(\frac{v_e'}{10c_{Ai}}\Big)^{-1/2} = 0.16\Big(\frac{\mathcal{E}'}{m_i c_{Ai}^2}\Big)^{-1/4}, \qquad (6)$$

where the prime sign $'$ denotes a physical quantity in a rest frame. Here we consider an appropriate rest-frame velocity $\boldsymbol{U}$, so that $\boldsymbol{v}_e' = \boldsymbol{v}_e - \boldsymbol{U}$. In this case, since the $\mathbf{E}\times\mathbf{B}$ velocity is non-uniform (Fig. 3a) and since $E_\parallel$ is finite (Fig. 3b), it is impossible to find out $\boldsymbol{U}$ that transforms away the electric field. We approximate $\boldsymbol{U}_{43.2} \approx (4, -3, 0)$ by referring to the $\mathbf{E}\times\mathbf{B}$ velocity at $z = \pm 0.22$–0.24, where $|E_z|$ hits its maximum (Fig. 3b). In this case, compared with the electron velocities in Figure 6d, the frame speed $|\boldsymbol{U}_{43.2}|$ is relatively small and so one can approximate $\mathcal{E}' \approx \mathcal{E}$. From Equation (6) and Figure 6c, one can see that $\kappa \sim \mathcal{O}(0.1)$ for the two electrons. This is reasonable, because the Speiser motion appears in the $\kappa \ll 1$ regime.

Regardless of whether they follow global or local Speiser orbits, we find that the electrons undergo either of the following two orbits after the Speiser phase. One follows a field-aligned outgoing orbit, like in the first red electron. This corresponds to the field-aligned electron outflow near the separatrix, discussed in Section IV. The other follows a chaotic bounce motion around the midplane, as evident in the second green orbit. It is located at $(x, z) = (50.0, -0.1)$ at $t = 35$ and so we discuss the electron motion near $x \sim 50$. This region corresponds the middle of a broader current layer of unmagnetized ions.[34,66] The electric current is weaker, and therefore the magnetic curvature radius is larger than in the super-Alfvénic jet. We estimated the curvature radius $R_{\rm c,min} = 0.62$ at $x = 50.0$ and the frame velocity $\boldsymbol{U}_{50.0} = (1.37, -0.1, 0)$. The electric field is excellently transformed away. The electron maximum Larmor ra-

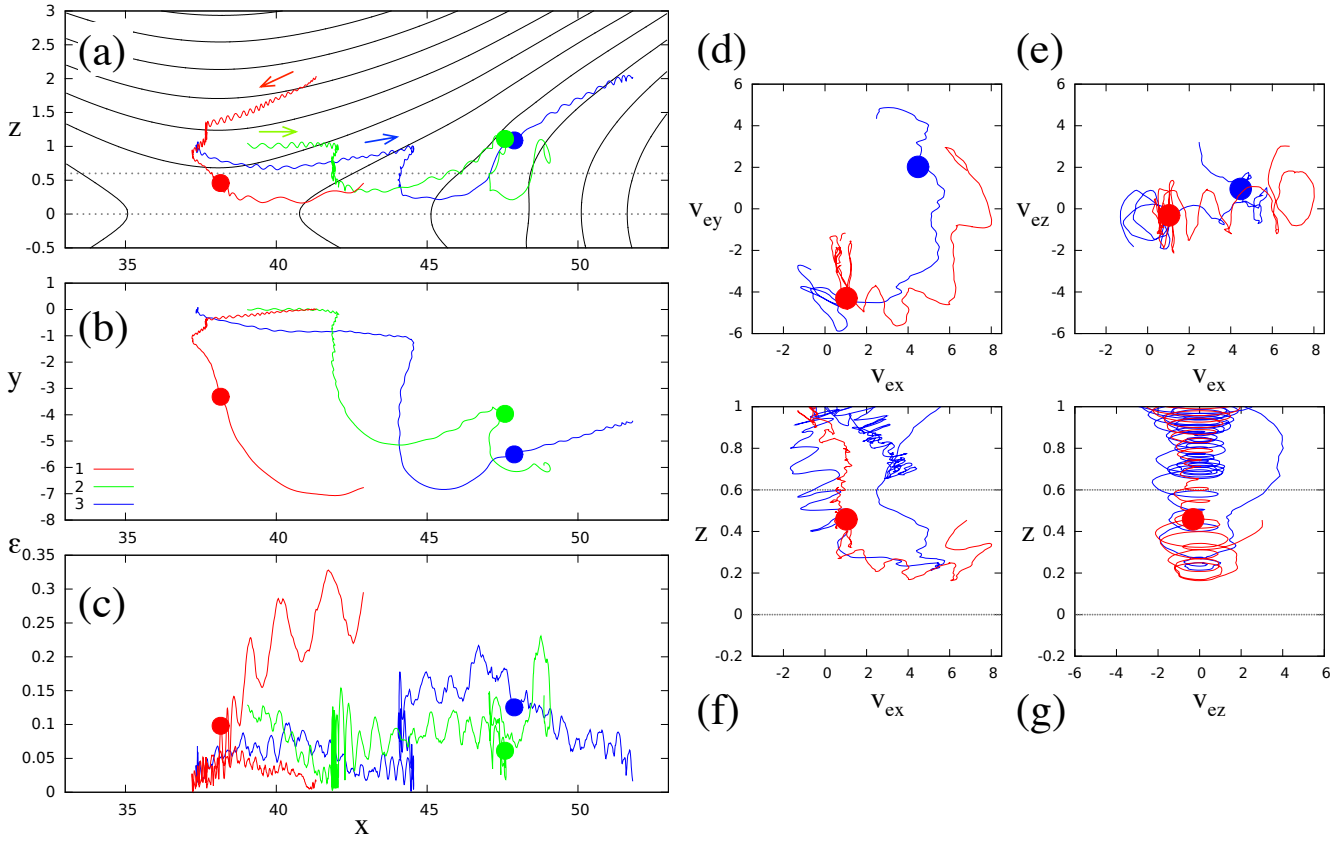

FIG. 7. (Color online) Noncrossing Speiser orbits in the same formats as in Figure 6. The right panels focus on the first (red) and the third (blue) electrons. The velocity paths (d,e) are computed in the rage of $0 < z < 0.6$ between the two dotted lines.

dius and the curvature parameter are,

$$\frac{r_{\rm L,max}}{d_i} \approx 0.83\Big(\frac{\mathcal{E}'}{m_i c_{Ai}^2}\Big)^{1/2}, \quad \kappa \approx 0.86\Big(\frac{\mathcal{E}'}{m_i c_{Ai}^2}\Big)^{-1/4}. \quad (7)$$

One can approximate $\mathcal{E}' \approx \mathcal{E}$, because the frame speed $|\boldsymbol{U}_{50.0}| = 1.37$ is negligible. One can see $\kappa \lesssim 1$ from Figure 6c. Figure 6a tells us that the typical bounce width $|z| \sim 1$ is comparable with $R_{\rm c,min} = 0.62$. In this regime, the particle motion becomes highly variable. Although we do not track the orbit long enough, the third blue electron exhibits a similar nongyrotropic motion around $x \gtrsim 48$.

B. Noncrossing Speiser orbits

In Figure 7, we show a new class of electron orbits in the same format as Figure 6. These electrons approach the midplane $z = 0$ and then all of them exhibit Speiser-like rotations in the x–y plane (Fig. 7b). During the motion, particles bounce in z. However, surprisingly, they do not cross the midplane (Fig. 7a). To guide our eyes, we indicate $z = 0$ and $z = 0.6$ by the dotted lines in Figures 7a, 7f, and 7g. One can see that all orbits are above the $z = 0$ line. Owing to this, we call them "noncrossing Speiser orbits." Strictly speaking, there is no guarantee that the reconnecting magnetic field changes its polarity at the midplane, $z = 0$. However, we confirm that the midplane is fairly identical to the field reversal, because of the perfectly symmetric configuration in z and a large number of particles per cell in our simulation. In panels in Figure 2, the dashed line indicates the field reversal, $B_x = 0$. One can see that it is located at $z \approx 0$ and that it is sometimes slightly *below* the midplane ($z < 0$) near the remagnetization front. This provides further confidence that these electrons do not cross the field reversal plane.

First, we examine the motion of electron #1 in red. It starts from the upper inflow region (Fig. 7a). Since there is a reconnection electric field E_y, it drifts in $-z$ at the speed of $-E_y/B_x$ while traveling along the field line. Once it reaches the $0.3 \lesssim z \lesssim 0.8$ region above the DR, it travels in the $-y$ direction. Its energy starts to increase (Fig. 7c). The $-y$-motion is attributed to the $\mathbf{E}\times\mathbf{B}$ drift by the polarization electric field E_z.[17,35] The gyrocenter velocity approaches $(0, E_z/B_x, -E_y/B_x)$, which becomes faster in the closer vicinity of the midplane, because the magnetic field decreases $B_x \to 0$. This drift motion in $-y$ is also evident in Figure 5a. Note that E_z is negative here (Fig. 2c). At $t = 35$, the electron is located at $(x, z) = (38.15, 0.46)$ with the velocity of $\boldsymbol{v}_e = (1.0, -4.3, -0.06)$.

(a) Trajectory in the velocity space

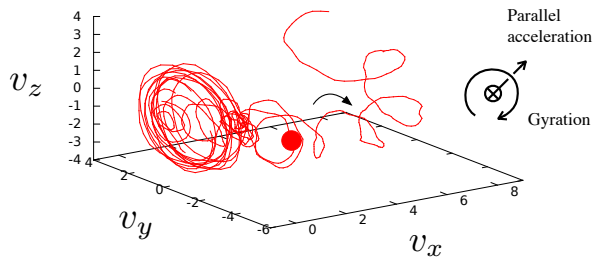

(b) Conceptual model

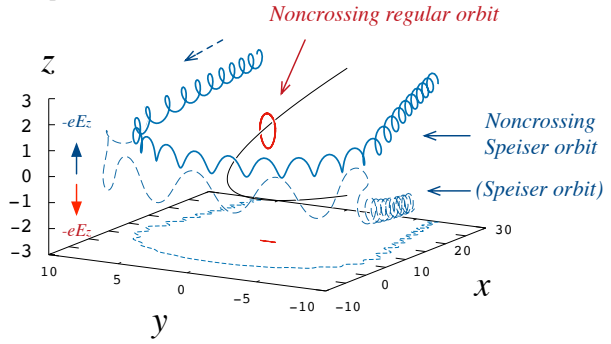

(c) Conceptual model - velocity space

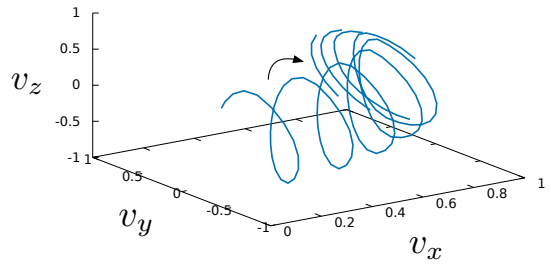

FIG. 8. (Color online) (a) Trajectory of the electron #1 in the 3D velocity space. (b) A conceptual model of noncrossing electron orbits. A noncrossing Speiser orbit (solid line) and a noncrossing regular orbit (red). They are computed in a configuration similar to the traditional Speiser orbit (dashed line) in Figure 1. (c) Velocity-space trajectory of the noncrossing Speiser orbit for $y < 0$ and $z < 1.5$.

Below this position, the electron starts to turn to the outflow direction (Fig. 7b) above the midplane. Figures 7d and 7e present the velocity-space trajectories within $0 < z < 0.6$. The velocity for the electron #1 rotates anti-clockwise in v_x–v_y (Fig. 7d), turning to the outflow direction. During this phase, the electron bounces in z (Figs. 7a and 7e). These features are similar to those in the Speiser motion.

We further examine the orbit #1 in the 3D velocity space (Fig. 8a). One can see that the velocity vector keeps rotating in the same direction. This tells us that the electron motion is a combination of a gyration and a guiding-center motion. It is apparently different from the conventional Speiser motion with a meandering motion, which exhibits the zigzag pattern in the velocity space (Fig. 1b). In Figure 8a, the spiral path further indicates that the electron is continuously accelerated in the parallel direction. We confirm that the electron #1 is accelerated by a parallel electric field, by reconstructing the electromagnetic field at the particle position. Except for minor noises, the parallel field $E_\parallel$ points inward to the X-line, continuously accelerating the electron away from the X-line in $+x$. This is consistent with the spatial profile of $E_\parallel$ (Fig. 2d). In the case of the electron #1, the parallel acceleration is responsible for the most of the energy gain, in particular at the later stage. On a longer time scale, the electron velocity slowly rotates anti-clockwise in v_x–v_y (Fig. 7d). One can also interpret that the electron slowly gyrates about B_z, while the E_z field prevents the particle from crossing beyond a certain distance in z. Note that a field-aligned component $E_\parallel$ is a projection of the polarization electric field E_z. Summarizing these results, this orbit is similar to but different from the traditional Speiser orbit, in the sense that it relies on a combination of the drift motion and the parallel acceleration instead of the meandering motion. Hereafter we call the orbit the "*noncrossing* Speiser orbit."

The second (green) and third (blue) orbits in Figure 7 are other examples of the noncrossing Speiser orbits. The electron #2 exhibits multiple reflections in the z direction. After entering the central region at $x \approx 42$, it slowly turns to the $+x$ direction, travels upward at $x \approx 47$, and then comes back to the central channel once again. It travels fast in x and in $-y$ near the midplane due to the $\mathbf{E}\times\mathbf{B}$ drift by the Hall field E_z (Figs. 2c and 2e), while it slowly moves in the pedestal region outside the electron jet. The electron #3 in blue travels backward along the field lines into the central channel at $x = 44$, and then it drifts in the $-y$ direction due to the Hall field E_z. The initial energy of this electron is very low. It is accelerated to the $\mathbf{E}\times\mathbf{B}$ speed $\approx |E_z/B|$ in this jet flank region. Then the electron turns round to $+x$ around $44 < x < 47$. One can also see the spiral in the velocity spaces (Figs. 7d and 7e), indicating a parallel acceleration by $E_\parallel$. Finally, the electron escapes upward along the field lines.

We verify the forces acting on the noncrossing Speiser-orbit electrons using a conceptual model. To mimic the Hall field E_z, we impose $\boldsymbol{E} = -|v_{e0}|B_0 \sin(\pi z/L)\boldsymbol{e}_z$ near the midplane ($|z| < L$) to the parabolic model in Section II. Here, $|v_{e0}| = 1$ is the initial electron velocity outside the Hall-field region ($|z| > L$). Corresponding electrostatic potential $\int_0^L |E_z| dz = 2/\pi$ is sufficient to reflect electrons whose normalized energies are $\frac{1}{2}m_e|v_{e0}^2| = 0.5$. Figure 8b displays test-particle orbits in the modified field. The blue orbit (solid line) employs the same initial condition as the Speiser-orbit electron (dashed line) in Figure 1a. As can be seen, it excellently reproduces qualitative features for noncrossing Speiser orbits. The electron remains on the upper half due to the electric field, turns its direction, and then exits in the $+x$ direction. Figure 8c shows the velocity-space trajectory, when the electron is in the right half ($y < 0$) around the midplane ($z < 1.5$). It exhibits a similar spiral of the $\mathbf{E}\times\mathbf{B}$

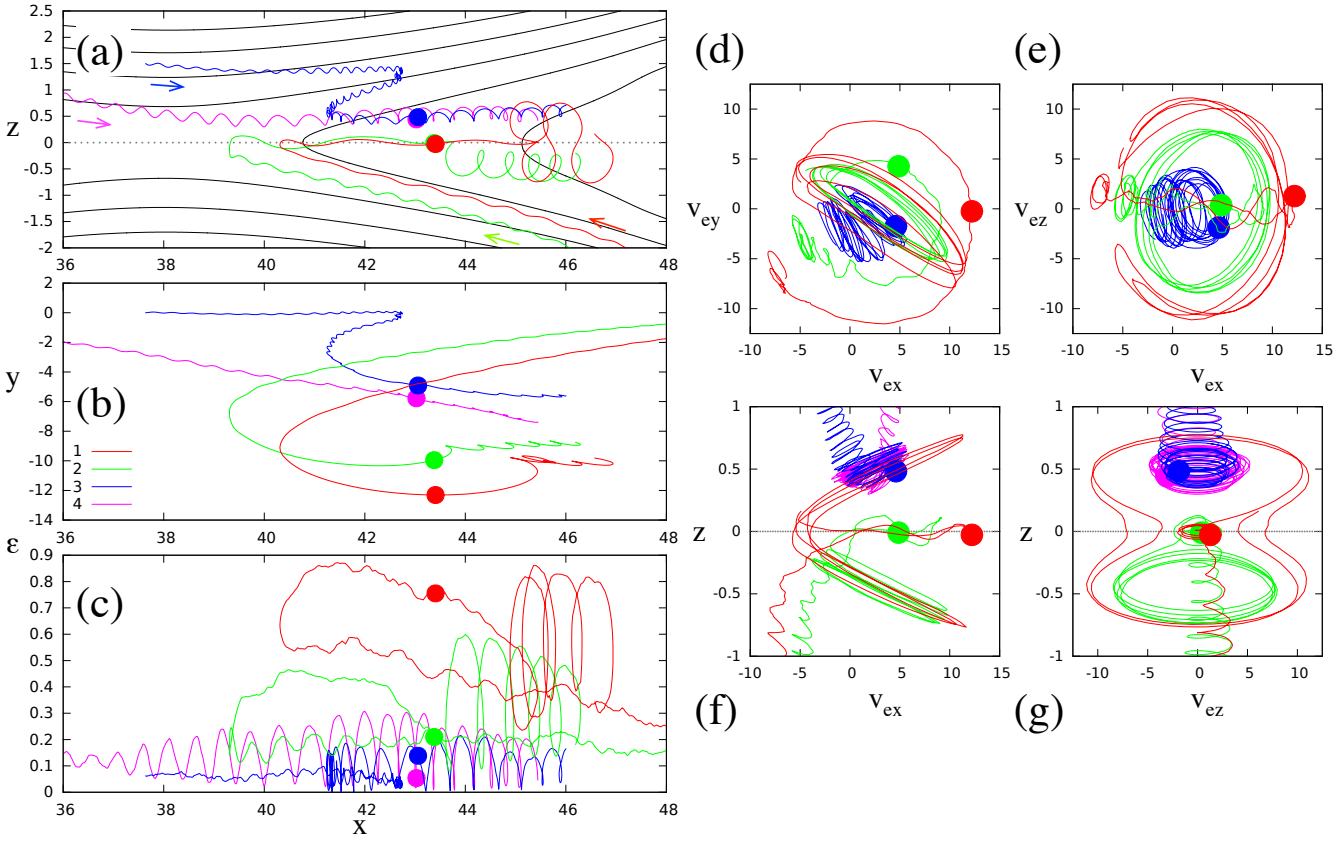

FIG. 9. (Color online) Trapped electrons in the same formats as in Figure 6. The velocity paths (d,e) are computed in the rage of $-1 < z < 1$. The 4th electron in purple is not shown in (d) and (e).

drift and the parallel motion as in Figure 8a.

We note that these noncrossing electrons have lower energy than the Speiser electrons in Section VI A. If electrons have enough energies, they will cross the midplane. Among the three, the first one gains the highest energy, probably because B_z is weak near the X-line. Its radius in the x–y plane (Fig. 7b) is the largest. The other two are picked up by the outflow exhaust and then they are locally reflected above the midplane. All these features are similar to the Speiser orbits, even though electrons are always reflected upward by the Hall field E_z or by the parallel electric field $E_\parallel$ above the midplane at $z = 0.2$–0.4 (Figs. 2c and 3b). In analogy with the conventional Speiser orbits, we classify the first one as the noncrossing global Speiser orbit, and the other two as the noncrossing local Speiser orbits.

C. Regular orbits

Figure 9 presents electron orbits of another kind in the same format as in Figure 6. The first one in red originally comes from the bottom right and then undergoes the local Speiser motion. The velocity vector rotates anti-clockwise in v_x–v_y (Fig. 9d) and then the electron eventually turns in the $-x$ direction. Very interestingly, it starts to bounce in z at $x > 45$. This orbit looks stable. We argue that this is a regular orbit in a curved magnetic geometry (Section II). The diagonal oscillation in v_x–v_y (Fig. 9d), the inverse C-shaped oscillation in v_x–v_z (Fig. 9e), and the V-shaped path in the phase space (Fig. 9f) suggest a trapped motion in an appropriately moving frame. The diagonal oscillation is transverse to the magnetic fields outside the electron current layer. The characteristic closed circuit in the v_z–z space (Fig. 9g) is consistent with the regular orbit in Figure 1d (the red orbit). At $x = 45.6$, the curvature radius is $R_{\rm c,min} = 0.079$ and the normal magnetic field is $B_z = 0.069$. The corresponding curvature parameter is

$$\kappa \approx 0.23\Big(\frac{v_e'}{10c_{Ai}}\Big)^{-1/2} = 0.20\Big(\frac{\mathcal{E}'}{m_i c_{Ai}^2}\Big)^{-1/4}. \qquad (8)$$

In this case, it is difficult to estimate the reference-frame velocity $\boldsymbol{U}$, because the ideal velocity $\boldsymbol{w}$ has the variation in z (Fig. 2e). We roughly evaluate $v_e' = 7.5$–10 (Fig. 9e) and $\mathcal{E}' \approx 0.7$ (Fig. 9c), and then obtain $\kappa \approx 0.2$.

In the second case, the green electron enters the DR and then undergoes a global Speiser motion. After leaving the midplane at $x = 43.7$, it starts gyrating in the lower half. The orbit looks similar to the first regular orbit in red in the phase spaces (Figs. 9f and 9g), except that the electron always remains below the midplane.

Figures 2c–2d suggest that the Hall field E_z keeps the electron away from the midplane. Without E_z or $E_\parallel$, an electron usually crosses the midplane in such a field configuration, because it is reflected by the mirror force toward the midplane. This electron keeps gyrating around $z \sim -0.5$, because it is also mediated by the Hall field E_z. We argue that this is a noncrossing variant of the electron regular orbit. It is detached from the midplane, due to the Hall field E_z.

Both the third electron in blue and the last electron in magenta travel through similar stable orbits. The blue one comes from the inflow region and then enters the stable channel after crossing the separatrix. The magenta one directly enters the channel, traveling above the X-line. They keep gyrating on the upper flank of the electron jet region (Figs. 9a, 9f, and 9g). They have lower energies than the previous two cases. One may interpret these electrons as just drifting. This is a good point, but we remark that drift motions have no influence in the parallel motion. These electrons are trapped in the parallel direction, balanced by the mirror force toward the midplane and the parallel electric force $-eE_\parallel$ away from the midplane. We verify the forces on these orbits using the test-particle model in Section VI B. A stable orbit is shown in red in Figure 8b. Therefore, it is appropriate to call the orbits the noncrossing regular motions, rather than drift motions.

Theoretically, the figure-eight-shaped regular orbits exist in the field reversal for $\kappa \lesssim 0.53$.[60] However, we find the figure-eight-shaped regular orbits only for $\kappa \lesssim 0.2$. We attribute to this to the Hall electric field E_z, which remains finite in the moving frame. Keeping electrons away from the midplane, E_z delays the z-bounce motion. Recalling that κ is the frequency ratio of the gyration about B_z to the z-bounce motion, the Hall field E_z increases an effective κ and therefore the threshold is reduced to $\kappa \approx 0.2$. One can also interpret in the following way: While lower-κ (higher-energy) electrons are insensitive to E_z, higher-κ (lower-energy) electrons are sensitive. The Hall field E_z transforms the high-κ figure-eight-shaped orbits ($0.2 \lesssim \kappa \lesssim 0.5$) to the noncrossing regular orbits. In Figures 9c–9e, one can see that all the noncrossing regular electrons have lower energy than the crossing electron in red in an appropriate frame. Although κ is not so meaningful for the noncrossing electrons, we plug in their typical velocities to Eq. 8 to obtain $0.2 \lesssim \kappa \lesssim 0.4$. This further suggests that they are detached variants of the regular orbits.

VII. COMPOSITION ANALYSIS

The trajectory dataset allows us to explore kinetic signatures in further detail. Figure 10 shows the velocity, energy, and phase-space distribution of electrons at $t = 35$. Each symbol stands for the electrons in the dataset. Based on their trajectories, we classify the electrons into the following three classes. The green circles indicate electrons that never cross the midplane $z = 0$ during the interval ($30 < t < 36.25$). We call them "noncrossing candidates." They may cross the midplane before $t = 30$ or after $t = 36.25$. The red triangles indicate electrons that spent some time in the square region of $x, z \in [35.5, 40.5] \times [-0.2, 0.2]$ during the interval. This region approximates the DR, which is indicated in Figure 2h. We call them "DR-crossing electrons." The blue crosses indicate the other electrons. They have crossed the midplane at least once, but they spent no time in the DR during the interval. We call them "crossing electrons." Please note that the frontmost symbols sometimes overwrite the background ones in panels in Figure 10. The order is carefully selected to emphasize interesting features.

Panels in the first three rows show the electron VDFs at $t = 35$. They are equivalent to those in Figure 4. Typical features of the separatrix VDFs are found in Figures 10b–d. In general, one can recognize outgoing red particles from the DR and incoming blue electrons toward the midplane. In Figure 10b, the leftmost electrons turn red, because they are going to enter the DR. Figure 10c contains the outgoing blue population, which crossed the midplane outside the DR. In Figure 10d, the outgoing red population is more prominent in the $v_{ex} > 0$ half, even though the outgoing blue population is also hidden behind them. This is reasonable because the electrons from the DR (global Speiser electrons) are more energetic than the local Speiser electrons, and therefore the DR-crossing electrons travel deeper into the exhaust region beyond the remagnetization front.

Surprisingly, we find a substantial amount of noncrossing candidates in the first four VDFs (Figs. 10a–d). In these panels, a number on the bottom-right corner indicates the ratio of the number of noncrossing candidates to the total number. In Figure 10a, right above the DR, 89% of the electrons are noncrossing candidates. The noncrossing candidates are also hidden behind the central red population. For example, the diamond symbol indicates the electron #1 in Figure 7. As discussed, it travels through the global noncrossing Speiser orbit. Here this electron is classified as noncrossing electrons in green. Interestingly, this electron also hits the DR of $x, z \in [35.5, 40.5] \times [-0.2, 0.2]$, even though it does not cross the midplane. In contrast, only a limited number of electrons are entering the DR and crossing the midplane. The red population is found only around the center $|v_{ex}| \sim 0$, while left-going and right-going populations are noncrossing. In the next domain (Fig. 10b), although some blue crosses are hidden behind the green circles, the noncrossing candidates are majority, accounting for 68% of the total electron number. The purple and magenta circles indicate the electrons #3 and #4 in Figure 9. As discussed in Section VI C, they are trapped on the upper flank of the electron jet, traveling through noncrossing regular orbits. The relevant blue orbit in v_x–v_z (Fig. 9e) is in excellent agreement with the green region in Figure 10b. These results suggest that the green noncrossing

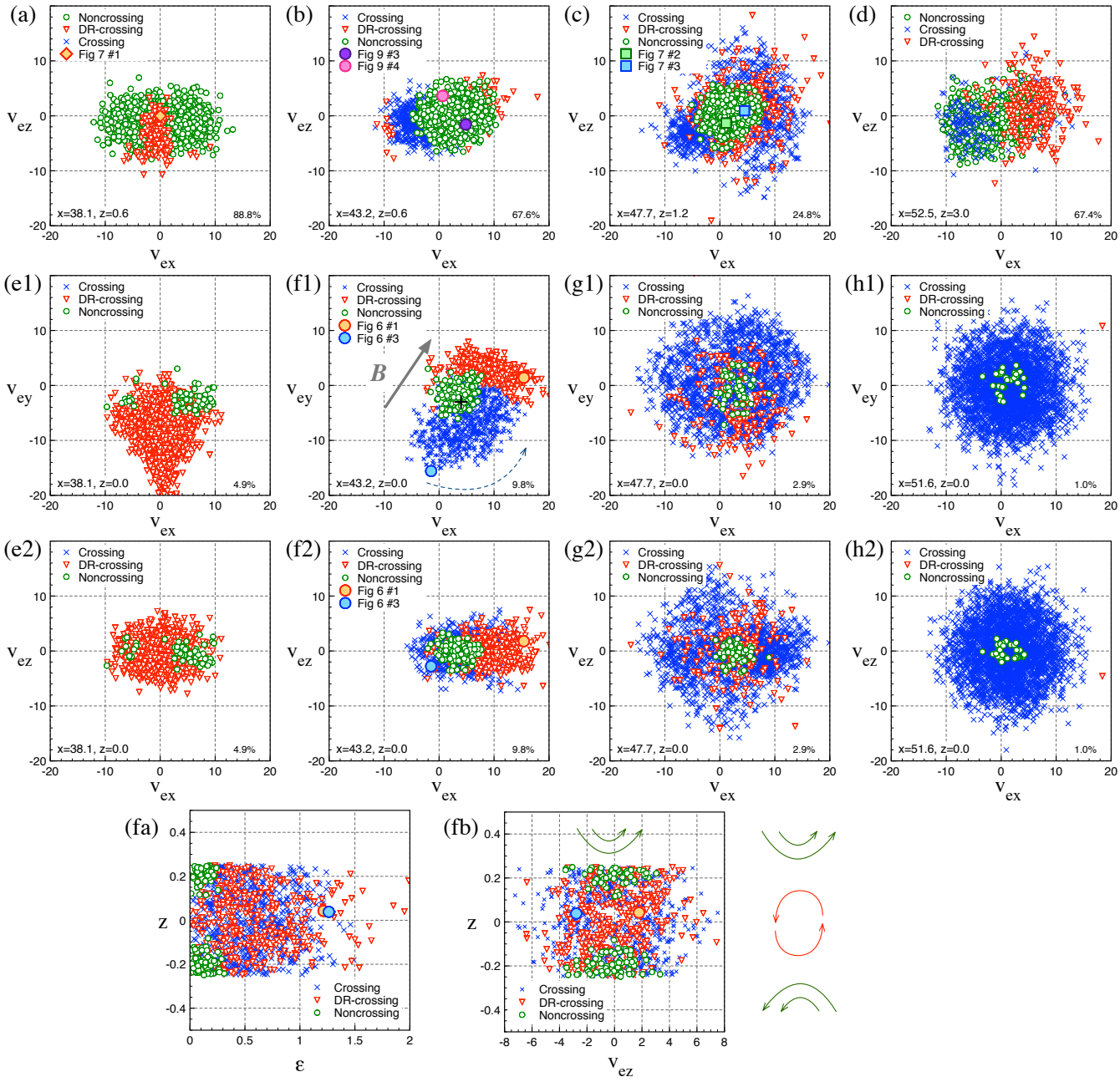

FIG. 10. (Color online) Composition of electron velocity distribution functions (VDFs) at $t = 35$. They are computed in a box size of 0.5×0.5. The box positions are indicated in Figure 2a. (a-h) Electron velocity distribution functions (VDFs) in the same format as in Figure 4. (fa) Energy-space distribution in $\mathcal{E}$–z (Fig. 5f), and (fb) phase-space distribution in v_z–z (Fig. 5e), computed in the (f) region $(x, z \in [42.95, 43.45] \times [-0.25, 0.25])$. The electrons are classified as noncrossing electrons (green circles), DR-crossing electrons (red triangles), and other noncrossing electrons (blue crosses). See the text for further detail.

population in Figure 10b are likely to travel through the noncrossing regular orbits.

Farther away from the DR, in Figure 10c, 25% of electrons are noncrossing candidates. The two squares indicate the noncrossing Speiser electrons #2 and #3 in Figure 7. They are either reflecting back to the midplane (#2) or escaping outward (#3). In this VDF, the noncrossing candidates are found around the center. Their velocity distribution is fairly unchanged from the previous case (Fig. 10b). The hot outgoing population consists of the crossing electrons in either red or blue. This suggests that they are Speiser-accelerated electrons from the midplane. One can see in Figure 6 that the Speiser-accelerated electron in red wraps around the magnetic field line along the separatrix (Fig. 6a). Its velocity (Fig. 6e) explains the hot population in Figure

10c very well. The hot population is evident in the (c) region and in further downstream along the separatrix, because Speiser electrons are ejected from the midplane at the end of the ECL, as can be seen in the orbit #3 (blue) in Figure 6a (See also Fig. 4(a) in Ref. 8). This agrees with the divergent flows in $\pm z$ (Fig. 2b; Sec. IV) and the vertically spread VDF (Fig. 4g; Sec. V).

In Figure 10d, we recognize green noncrossing candidates in the incoming direction ($v_x < 0$). Some are hidden behind the blue crossing electrons. These green candidates may be overemphasized, because the (d) region is far from the DR and the midplane. The field-line through $(x, z) = (52.5, 3.0)$ at $t = 35$ is convected to $(x, z) = (48.4, 0.0)$ at $t = 36.25$, and the field-aligned distance to the midplane is $\approx 5[d_i]$. The electrons at a velocity $|v_e| = 4$ will travel $5[d_i]$ from $t = 35$ to $t = 36.25$. Therefore, some green electrons could be crossing electrons. On the other hand, our classification will be valid in the outgoing part ($v_x > 0$). One can see energetic electrons from the DR in red. They are more pronounced than blue crossing populations. Importantly, the green population retains signatures similar to those in the previous cases. From these four panels, we find a non-negligible amount of noncrossing electrons. This will be further analyzed in this section.

Panels in the second and third rows show the VDFs at the midplane, similar to those in Figure 4. The left panels (Fig. 10e) indicate the VDFs around the X-line. We recognize some amount of green noncrossing electrons here, because the VDF is calculated in a thicker box in z than the square region to classify the red population, and because some noncrossing electrons come close to the midplane (e.g., the orbit #1 in Fig. 7a). Aside from them, the (e) region is filled with the DR-crossing electrons in red. As we depart from the X-line in the $+x$ direction, the blue population gradually replaces the red population in the VDFs. In the v_x–v_y space (Fig. 4f1), the blue population appears in the bottom ($v_{ey} < 0$). Then they evolve anti-clockwise, as the dashed arrow indicates. The red population rotates anti-clockwise accordingly. Finally, all these electrons are mixed with each other around the remagnetization front (Fig. 4g). We see no remarkable separation in color farther downstream.

In Figure 10f1, we argue that the global Speiser motion accounts for the DR-crossing electrons in red and that the local Speiser motion accounts for the other crossing electrons in blue. The two circles in Figure 10f indicate the representative electrons for the global Speiser motion (the orbit #1 in Fig. 6) and for the local Speiser motion (#3), discussed in Section VI A. For the local-type Speiser motion, we expect a half-ring distribution function in v_x–v_y, corresponding to the slow half-gyration about B_z. In Figure 10f1, the gray arrow indicates the orientation of the magnetic field at $z = 0.22$–0.24. It is tilted by 56 degrees due to the Hall effect. In Section VI A, we estimated the frame velocity $\boldsymbol{U}_{43.2} = (4, -3, 0)$. This is indicated by the black cross in Figure 10f1. Keeping these in mind, one can see that the blue electrons are distributed in a semicircle or a half ring surrounding $\boldsymbol{U}_{43.2}$ in this velocity space. The semicircle is tilted, similar to the magnetic field outside the ECL (the gray arrow). From Figures 10f1 and 10f2, one can see the typical velocity for the blue electrons $v_e' = |\boldsymbol{v}_e - \boldsymbol{U}_{43.2}| \approx 5$–$15\ c_{Ai}$, which corresponds to the Speiser regime of $\kappa < 1$ (Eq. 6). All these features are consistent with the Speiser motion of local-reflection type.

In the (f) region, the green noncrossing candidates are found near $\boldsymbol{U}_{43.2}$ in the velocity spaces. Their thermal velocity is smaller than in the upper (b) region, probably because they lose their energy due to the Hall field E_z. Some more signatures of the green noncrossing electrons are evident in the energy-space and phase-space diagrams for the electron distribution (Figs. 10fa and 10fb), which correspond to Figs. 5f and 5e. In contrast to the two crossing populations (blue and red), the green noncrossing candidates are found only outside the midplane $|z| \gtrsim 0.1$. Their energy is low, $\mathcal{E} \lesssim 0.3$, in agreement with small thermal velocity in the VDFs. By definition, particles move downward (upward) in the $v_{ez} < 0$ ($v_{ez} > 0$) region in the v_z–z space (Fig. 10fb). With this in mind, we see that the green electrons are reflected away from the midplane. They rotates anti-clockwise near the $v_z = 0$ axis, as indicated by the green arrows. These features are consistent with the noncrossing orbits in Section VI (see Figs. 7g and 9g).

Next, we investigate spatial distribution of the noncrossing candidates. Figure 11a shows the density of the noncrossing candidates, reconstructed from our 3% dataset, in the same color range as in Figure 2f. Around the ECL, there are three layers of (1) the high-density yellow layers in the inflow region, (2) the medium-density green layers near the separatrices, and (3) the blue cavity along the midplane. Comparison between Figures 2f and 11a tells us that the noncrossing electrons are the majority in the inflow region, in particular in the high-density yellow layer. The noncrossing electron density decreases in the medium-density green layers, but it is non-negligible ~ 0.1. The noncrossing electrons disappear in the downstream of the remagnetization front, $x \gtrsim 48$. We note that the noncrossing electron density could be underestimated in the flanks of the ECL at $45 \lesssim x \lesssim 47$. Even if some electrons do not cross the midplane at $t < 35$, once they cross the midplane somewhere in the downstream ($x \gtrsim 48$) during $35 < t < 36.25$, we count them as crossing electrons in our analysis. Despite these concerns, we recognize many noncrossing candidates.

The presence of noncrossing electrons implies that upper-origin and lower-origin electrons may not mix with each other across the ECL. Figure 11b shows the electron mixing fraction at $t = 35$, computed from the full PIC datasets. The fraction is defined in the following way

$$\mathcal{M} \equiv \frac{N_{\rm up} - N_{\rm low}}{N_{\rm up} + N_{\rm low}} \tag{9}$$

where $N_{\rm up}$ is the number density of electrons that were

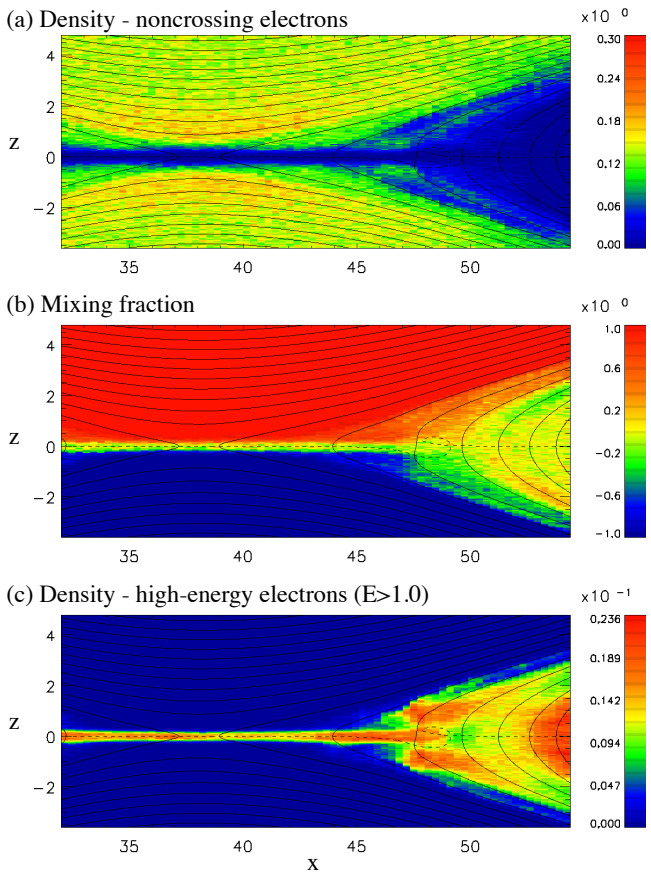

FIG. 11. (Color online) (a) Reconstructed density of the noncrossing electrons at $t = 35$. The color range is set similar to Fig. 2f. (b) Mixing fraction $\mathcal{M}$, defined by Eq. (9). (c) Density of the high-energy electrons for $\mathcal{E} > 1.0$.

in the upper half ($z > 0$) at $t = 30$ and $N_{\rm low}$ in the lower half ($z < 0$). It ranges from $\mathcal{M} \to +1$ in the upper inflow region to $\mathcal{M} \to -1$ in the lower region. During $30 < t < 35$, the magnetic flux across the X-line is transported by 1.7 in $\pm z$ and by 11.4 in $\pm x$. The latter is comparable with the distance between the X-line and the remagnetization front. Thus, we expect that electrons are fully mixed $\mathcal{M} \approx 0$ in the exhaust region between the separatrices. However, surprisingly, the electrons are mixed only inside the ECL in the upstream of the remagnetization front ($x \lesssim 48$). They are largely unmixed outside the ECL. Weakly mixed regions around $45 < x < 48$ between the ECL and separatrices do not change this picture. The electrons are quickly mixed in the downstream, $x \gtrsim 48$. Based on these results, we conclude that electron mixing is inefficient in the upstream side of the remagnetization front ($x \lesssim 48$) and that the electron mixing occurs mainly in the downstream of the remagnetization front.

Crossing electrons are distributed in the outflow region between the separatrices. Many of them follow the Speiser orbits. Through Speiser-type orbits, electrons can be accelerated to higher energies than the noncrossing electrons. Motivated by this, we examine the spatial distribution of energetic electrons. Figure 11c shows a number density of electrons whose energy exceeds a threshold, $\mathcal{E} > 1.0$. They are localized around the ECL ($x < 48$). The localization of the high-energy electrons is also evident in Figures 5c and 5f. They are crossing populations, as confirmed in Figure 10fa. These electrons follow either the global Speiser orbits from the DR or the local Speiser orbits that turn around inside the ECL. After the Speiser phase, these electrons escape along the separatrices or they chaotically remain around the midplane, as discussed in Section VI A. In Figure 11c, the energetic electrons are located on separatrices in the downstream of the remagnetization front ($47 < x < 53$). This supports the former (the orbit #1 in Fig. 6), while we do not see significant energization near the midplane. We find that some nongyrotropic electrons lose their energy as shown by the orbit #2 in Figure 6c. In these regions, Hoshino et al.[27] proposed a two-step mechanism of the Speiser acceleration and the ∇B acceleration. Our results are not favorable to the Hoshino et al.[27]'s proposal, probably because combinations of acceleration mechanisms vary from case to case. Farther downstream ($x > 52$), the energetic electrons are again found near the midplane. The region is equivalent to an outer edge of a long magnetic island, inside which these electrons are confined. We confirm that the energetic electrons are repeatedly accelerated inside the island across the periodic boundary in x.[12] Since we focus on electrons from the ECL side, these energetic electrons are out of the scope of this study.

In summary, a substantial amount of noncrossing electrons are found outside the ECL. They have less energy than the high-energy population inside the ECL, because the crossing electrons are accelerated via the Speiser process, once they enter the ECL. The energetic electrons exit from the ECL toward the separatrices.

VIII. OBSERVATIONAL SIGNATURES

We discuss potential observational signatures in this section. Figures 12a and 12b show electron energy-space spectrograms (E-S diagrams), computed from the PIC simulation at $t = 35$. We count the electron particle *flux* as a function of the logarithmic energy above the ECL at $z = 0.5$ (Fig. 12a) and along the ECL at $z = 0.0$ (Fig. 12b). The spatial resolution is $\Delta x = 0.89, \Delta z = 0.5$. The vertical axis is equivalent to the energy spectrum of $\mathcal{E}^{1.5} f(\mathcal{E}) d\mathcal{E}$. In Figure 12b, one can see a two-step profile of the electron count rates. The reconnection site ($18 < x < 59$) is filled with tenuous plasmas from the inflow region. The ECL ($28 < x < 48$) is embedded inside the region, as indicated by the dashed arrows. Around the X-line, we recognize many energetic electrons of $\mathcal{E} > 1$ (the solid arrow). Since they are absent above the ECL (Fig. 12a), they are quite probably accelerated near the X-line via the Speiser process.[47,55,62] The energy

spectrum has a power-law tail $f(\mathcal{E})d\mathcal{E} \propto \mathcal{E}^{-5.8}$ around the X-line. As we depart from the X-line in the ECL, the spectral index gradually decreases. The electron fluxes slightly shift to the higher energies and then shift to the lower energies. Another remarkable signature is the absence of the low-energy electron flux in the ECL. One can see that the electron flux of $10^{-1.5}$–10^{-1} suddenly disappears around the ECL in Figure 12b. In contrast, the low-energy electron flux remains fairly unchanged above the ECL (Fig. 12a).

The bottom two panels in Figure 12 show Geotail observation of magnetic reconnection from 0659:18 UT to 0708:16 UT on 5 May 2007. The satellite was located in the magnetotail at (-21.3, 6.9, 1.3 R_E) in the geocentric solar magnetospheric (GSM) coordinates at 0700 UT. This event was studied by Nagai et al.[38] in detail. Here we briefly introduce key signatures. Figure 12d presents the ion and electron bulk velocities, obtained from plasma moments. The x components of plasma perpendicular velocities are presented. Both the ion velocity ($V_{\perp x}$ in gray color) and the electron velocity ($V_{\perp x}$ in black) are initially negative, reverse their signs at 0702:41 UT, and then remain positive until ∼0707 UT. This and other signatures[38] suggest that the Geotail encountered bidirectional reconnection outflows in the close vicinity of the X-line. In the period 0701:17–0705:29 UT, the electron flow is decoupled from the ion flow. The shadow in Figure 12d indicates this ion-electron decoupling interval. Figure 12c shows electron counts per sample time in the energy-time (E-T) diagram. If the structure of the reconnection region is stationary, the E-S diagrams are equivalent to the E-T diagram. One can see that the electron fluxes shift to higher energies during the reconnection event from ∼0700 UT to ∼0707 UT. The dashed arrows indicated the ion-electron decoupling interval (0701:17 UT to 0705:29 UT). One can see that the electron fluxes shift to even higher energies and that the low-energy electron fluxes disappear.

We argue that the ion-electron decoupling interval corresponds to the ECL surrounding the X-line. The plasma velocities (Fig. 12d) are consistent with the super-Alfvénic electron jets (Fig. 2a). The profile of the E-T diagram (Fig. 12c) resembles the two-step profile of the E-S diagram (Fig. 12b). In particular, one can clearly see the two-step profile in the second half of the event; The inner ion-electron decoupling region (before 0705:29 UT) and the outer region (for example, 0705:29 UT – 0706:29 UT). The step-like transition is more evident in the observation, because we employ an artificially high electron temperature in the PIC simulation. Immediately after the flow reversal (0702:41 UT), the satellite observed the highest-energy electron flux, as indicated by the solid arrow in Figure 12c. This is consistent with the DR in PIC simulation (Fig. 12b). In the next few intervals, the highest-energy fluxes temporarily decreased, while the low-energy electron fluxes increased. Probably the electron flux in the pedestal region above the ECL (Fig. 12a) are contaminated, because the magnetic field was positive ($B_x > 0$; not shown) during the interval. In both PIC simulation and the satellite observation, we recognize the two-step profile of electron fluxes around the reconnection site. Both in the ECL and in the ion-electron decoupling interval, high-energy fluxes are found in the absence of the low-energy fluxes. The observation is consistent with our picture of the high-energy Speiser-accelerated electrons in the ECL and the low-energy non-crossing electrons outside the ECL.

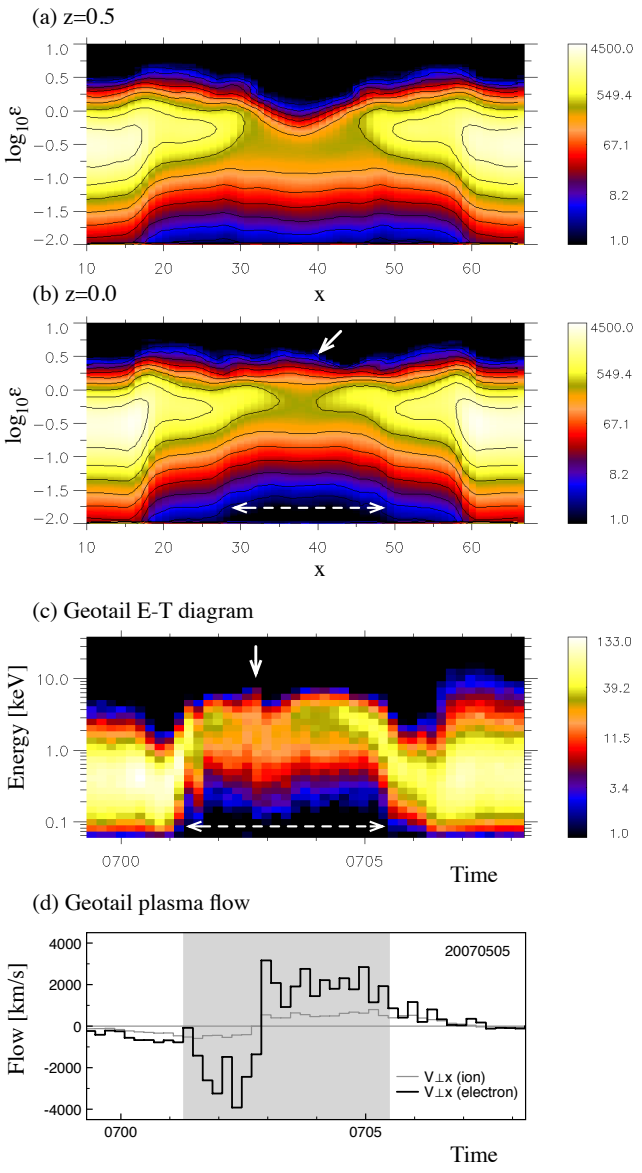

FIG. 12. (Color online) Electron energy-space spectrograms at $t = 35$ at two slices (a) $z = 0.5$ and (b) $z = 0.0$ in the PIC simulation. (c) Electron energy-time spectrograms and (d) plasma perpendicular flows, for the period from 0659:18 UT to 0708:16 UT on 5 May 2007, observed by the Geotail satellite.[38]

IX. DISCUSSION AND SUMMARY

We have investigated the basic properties of the ECL from various angles: Fluid quantities, VDFs, trajectories, and compositions. This allows us to understand the physics in and around the ECL much more deeply than before. For example, in the electron jet, we have found that the electrons are in the $\kappa \lesssim 1$ regime. They are unmagnetized, and follow Speiser orbits. Our orbit analysis and composition analysis suggest that the electron VDF consists of the following two Speiser populations. One is a global-type Speiser motion traveling through the DR, and the other is a local-type Speiser motion picked-up by the outflow exhaust. Since the Speiser electrons gyrate about B_z for a half gyroperiod near the midplane, the average electron velocity can be faster in x than the $\mathbf{E}\times\mathbf{B}$ velocity, $V_{ex} \approx V_{e\perp x} > w_x$, when the reconnecting magnetic fields have out-of-plane $\pm y$ components. This results in the violation of the electron ideal condition, $\boldsymbol{E} + \boldsymbol{V}_e \times \boldsymbol{B} \neq 0$ in the electron jet.[30,44,50] In addition, since electrons travel through chaotic or Speiser orbits, the VDF is no longer gyrotropic, and therefore the jet is marked by the nongyrotropy measures.[1,49,57] The z-bounce motion during the Speiser motion is responsible for the phase-hole in v_z–z (Fig. 5e), similar to the DR (Fig. 5b).[8,26] Since the z-bounce speed is smaller than the rotation speed in the x–y plane, one can see an electron pressure anisotropy with a stronger perpendicular pressure.[32]

Hesse et al.[23] argued that the super-Alfvénic electron jet speed can be explained by diamagnetic effects. They showed that the force balance is similar to the diamagnetic drift and that the z-profile of the off-diagonal component of the pressure tensor can be fitted by a gyrotropic pressure model. During the Speiser motion, electrons exhibit the meandering motion. It is plausible to categorize the meandering motion as the diamagnetic drift, because the diamagnetic drift is not a guiding center drift. However, it may not be the best way to discuss a gyrotropic pressure model inside the ECL,[23] because most electrons are in the unmagnetized regime of $\kappa < 1$. It is more appropriate to say that "nongyrotropic electrons carry the diamagnetic-type electric current" in the ECL.

For ions, similar semicircle or half-ring-type VDFs by Speiser motions were reported by hybrid simulations,[36,39] PIC simulations,[18,25,66] and satellite observations.[25] In particular, Ref. 66 discussed impacts of Speiser VDFs in PIC simulations in detail. They attributed a slow ion flow at a sub-Alfvénic speed and the violation of ion ideal condition to Speiser orbits. In this work, we attribute both a fast electron flow at a super-Alfvénic speed and the violation of electron ideal condition to Speiser motion. Ion physics and electron physics are similar, but some apparent effects are opposite: The ion flow looks slow while the electron flow looks fast. Ref. 66 further argued that some ions travel through figure-eight-shaped regular orbits.[5] We support this discovery by presenting electron regular orbits. The V-shaped path (Fig. 9f) corresponds to a narrow ion channel in the phase-space diagrams (Figs. 6b and 11b in Ref. 66). Therefore, both Speiser orbits and regular orbits appear in the nongyrotropic region in magnetic reconnection, regardless of plasma species.

We have further introduced a new family of electron orbits, the noncrossing orbits. They are attributed to the polarization electric field E_z. Particle motions are organized in a conceptual model in Figure 8b. Similar to conventional orbits, there exist the noncrossing Speiser orbits and the noncrossing regular orbits. The noncrossing Speiser orbits can be further classified into noncrossing global Speiser orbits and noncrossing local Speiser orbits (Sec. VI B). As seen in VDFs in Figure 10, the noncrossing electrons are confined in a low-energy part of the VDFs. They are the majority in number density (Fig. 11a). One can order-estimate a typical energy of the noncrossing electrons ($\mathcal{E}_{\rm NC}$) in the following way: Considering that the plasma density is nearly uniform over the reconnection site ($\sim n_b$; Fig. 2f), we obtain $n_b(T_i + T_e) \approx \frac{1}{2\mu_0}B_0^2$ from the pressure balance across the ECL. We find that ions sustain most of the perpendicular pressure. Since the ion bounce motion sustains the polarization field, the electrostatic potential energy should be a small fraction (δ) of the ion energy, $\delta \lesssim \mathcal{O}(0.1)$. The noncrossing electron energy satisfies $n_b\mathcal{E}_{\rm NC} \lesssim \delta n_b T_i \approx \delta\frac{1}{2\mu_0}B_0^2$. This yields $\mathcal{E}_{\rm NC} \lesssim 2.5\delta\, m_i c_{Ai}^2$, in agreement with $\mathcal{E}_{\rm NC} \lesssim 0.25$ in Figures 5c, 5f, and 10fa.

From the macroscopic viewpoint, the noncrossing electrons challenge the conventional understanding of (1) electron mixing and (2) electron heating during magnetic reconnection. First, as discussed in Section VII, the high-energy electrons from the two inflow regions mix with each other in the ECL. On the other hand, the noncrossing electrons do not enter the ECL due to the Hall field E_z. They start to mix with each other only downstream of the remagnetization front (Fig. 11b), where the Hall field E_z disappears (Fig. 2c). In Figure 2h, we recognize the enhanced energy dissipation around the DR, where the high-energy global Speiser electrons start to mix with each other, and near the remagnetization front (indicated by a circle), where the noncrossing electrons start to mix with each other. It is interesting to see that the nonideal energy transfer corresponds to these sites of electron mixing. The relevance between the dissipation measure $\mathcal{D}_e$ and electron mixing deserves further research. Second, the electron heating mechanisms have been actively studied in the last few years.[21,43,51] These works reported electrons parallel heating outside the ECL inside the outflow exhaust. They implicitly assume the local-type Speiser motion, while the relevant self-consistent orbits have not been investigated. In fact, Haggerty et al.[21] showed in Figure 2(d) of their paper that the electron jet region, flanked by the bipolar $E_\parallel$ layers, extends $40d_i$'s away from the X-line. This is favorable for the noncrossing electrons. We expect that the noncrossing electrons are an integral part of the electron VDFs of the exhaust region. The electron heating

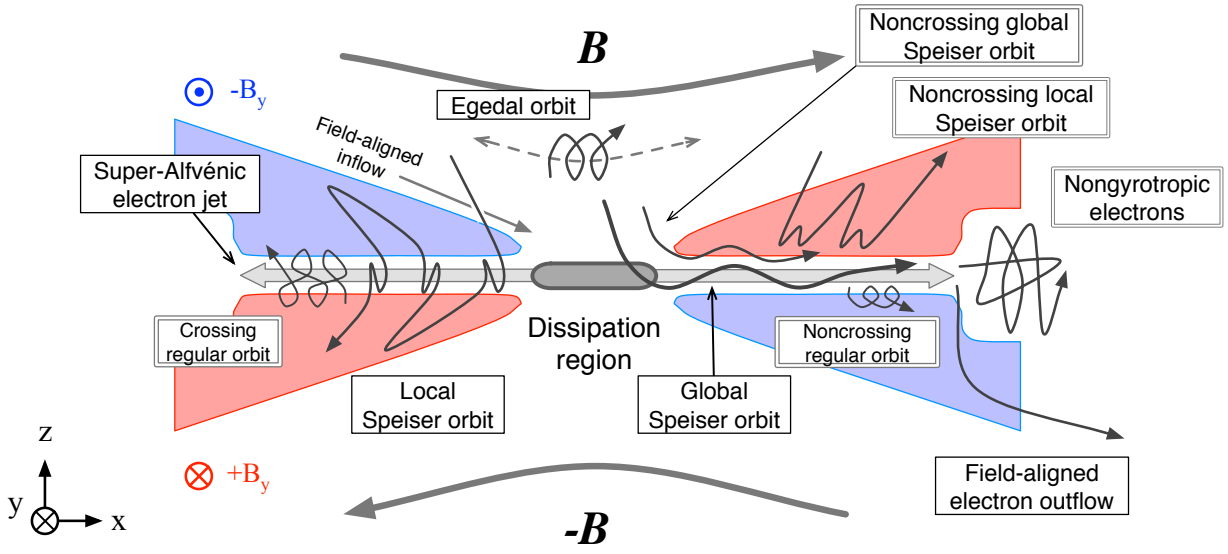

FIG. 13. (Color online) A schematic diagram of electron orbits near the reconnection site.

mechanism should be investigated in more detail, by considering the noncrossing electrons.

A question is whether these results are applicable to magnetic reconnection in the actual magnetotail, because we have employed artificial parameters in our PIC simulation. The parameters include the mass ratio (m_i/m_e), the density ratio (n_b/n_0), the ratio of the plasma and gyro frequencies (ω_{pe}/Ω_{ce}), and plasma beta (β) in the inflow region. The mass ratio controls the relative size of the ECL within the reconnection site. However, as long as the ECL is well resolved, there is no reason to alter the electron physics. We expect that our results scale to the real mass ratio. Since tenuous inflow plasma occupies the reconnection site, the density ratio (n_b/n_0) should control only the build-up time of the ECL structure. The frequency ratio (ω_{pe}/Ω_{ce}) in the inflow region will be important, because it controls electrostatic properties around the ECL.[9,29,35,64] We expect that the Hall field $|E_z| \sim c_{Ae,in}B_0 = (\omega_{pe,in}/\Omega_{ce})^{-1}cB_0$ will be important for $(\omega_{pe}/\Omega_{ce}) \sim \mathcal{O}(1)$. As we estimated in Ref. 64, the inflow frequency ratio in our PIC simulation is

$$\frac{\omega_{pe,in}}{\Omega_{ce}} = \frac{\omega_{pe}}{\Omega_{ce}}\left(\frac{n_b}{n_0}\right)^{1/2} \approx 1.8. \qquad (10)$$

In the tail lobe, we expect $\omega_{pe,in}/\Omega_{ce} = 1.6$–$2.3$ for $B = 20$ nT and $n_b = 0.01$-0.02 cm^{-3}. Thus, our results will be applicable to the magnetotail reconnection. The plasma beta β, in particular, the electron beta $\beta_e \equiv 2\mu_0 p_e/B^2$, may be another important factor. In the cold limit of $\beta_e \to 0$, as in the magnetotail, we expect that fine structures will be more evident in electron VDFs.[2,53]

The noncrossing electrons can be more pronounced in magnetic reconnection in different configurations. We address two favorable cases of driven-type reconnection and asymmetric reconnection. In the so-called driven systems, inflow plasmas are continuously injected toward the reconnection site. In such a case, the ions interpenetrate deeper than in the undriven case and therefore the polarization electric field becomes stronger. Then we expect more noncrossing electrons on both sides of the midplane. In fact, Horiuchi & Ohtani[26] presented an electron phase-space diagram across the X-line in a PIC simulation of driven reconnection (Fig. 5 in Ref. 26). The diagram shows clear signatures of noncrossing electrons, two high-density electron regions in red inside the ion meandering region. In asymmetric systems, there is often a density gradient across the two inflow regions. Previous PIC simulations[48,58] reported a strong normal electric field on the low-density side of the boundary layer. This is a polarization field and this electric field layer overlaps the DR. In such a case, the low-density side of the DR is very favorable for noncrossing electrons. At the Earth's magnetopause, magnetic reconnection takes place between a high-density magnetosheath plasma and a tenuous magnetospheric plasma, continuously driven by the solar wind. We expect that noncrossing electrons will be a key player for understanding the physics of magnetopause reconnection. Since the sunward polarization electric field will be enhanced, magnetospheric electrons will rarely mix with magnetospheric plasma in the exhaust region.

In addition, the reconnection system may involve an out-of-plane magnetic field (the so-called guide-field). In fact, reconnection events with a guide-field have been observed even in the Earth's magnetotail,[14] where we expect antiparallel magnetic fields. Since a small guide-field alters the ECL structure,[33,46,56] the noncrossing electron orbits will be modified accordingly. A guide-field tends to magnetize electrons even in the DR, while the polarization electric field persists in the guide-field case. Electron orbits in guide-field reconnection deserve inde-

pendent research. We have also ignored the variation in the y direction. At this point, it is not clear whether our picture persists in 3D configurations or not. Nevertheless, it is encouraging that the satellite observation is consistent with the simulation with noncrossing electrons (Sec. VIII).

In this work, we have investigated particle dynamics in the electron current layer (ECL) in collisionless magnetic reconnection in an antiparallel magnetic field. By tracking self-consistent trajectories in the two-dimensional PIC simulation, we have found new classes of electron orbits. The electron motion in and around the ECL is much more complicated than we have expected before. The new orbits, as well as previously known orbits, are schematically illustrated in Figure 13. In the inflow region, electrons are gyrating and fast-bouncing in the parallel direction, as extensively studied by Egedal et al. [15,16]. Near the separatrices, some electrons stream along the field lines toward the X-line. Once electrons enter the DR, they undergo the Speiser motions of global type.[55] The electrons slowly turn around to the outflow directions while bouncing in z. Others travel through the Speiser motions of local-reflection type. Inside the ECL, there exists an figure-eight-shaped (crossing) regular orbit.[5,66] The polarization electric field introduces noncrossing regular orbits on the jet flank and noncrossing Speiser orbits. Similar to the traditional Speiser orbits, the noncrossing Speiser orbits can be categorized as the global type and the local reflection type, although their difference is ambiguous. Downstream of the remagnetization front, some Speiser electrons remain around the center as nongyrotropic electrons, while others travel near the separatrices in field-aligned electron outflows.

Considering particle orbits, we have discussed key properties of the electron jet. The electrons are traveling through Speiser orbits. The fast bulk speed, electron nonidealness, anisotropy, and nongyrotropy are consequences of the electron nongyrotropic motion in the $\kappa \lesssim 1$ regime. The noncrossing orbits are consistent with the electron density profile, the energy-dependent spatial distribution of electrons, and the electron mixing sites with nonideal energy transfer. They correspond to the following observational signatures of the ECL: (1) The super-Alfvénic electron jet will be populated by high-energy nongyrotropic electrons. (2) The electron density is lower than in the jet flank region. (3) The electron energy-time diagram will exhibit the two-step profile. We hope these predictions will be confirmed by the MMS spacecraft[4] in the second science phase targeting the magnetotail.

ACKNOWLEDGMENTS

The authors acknowledge I. Shinohara for comments. This work was supported by Grant-in-Aid for Young Scientists (B) (Grant No. 25871054). The authors acknowledge facilities at Center for Computational Astrophysics, National Astronomical Observatory of Japan.

[1] N. Aunai, M. Hesse, and M. Kuznetsova, Phys. Plasmas **20**, 092903 (2013).
[2] N. Bessho, L.-J. Chen, J. R. Shuster, and S. Wang, Geophys. Res. Lett. **41**, 8688, doi:10.1002/2014GL062034 (2014).
[3] J. Büchner and L. M. Zelenyi, J. Geophys. Res. **94**, 11821, doi:10.1029/JA094iA09p11821 (1989).
[4] J. L. Burch, T. E. Moore, R. B. Torbert, and B. L. Giles, Space Science Reviews **199**, 5 (2016).
[5] J. Chen and P. J. Palmadesso, J. Geophys. Res. **91**, 1499, doi:10.1029/JA091iA02p01499 (1986).
[6] L.-J. Chen, N. Bessho, B. Lefebvre, H. Vaith, A. Fazakerley, A. Bhattacharjee, P. A. Puhl-Quinn, A. Runov, Y. Khotyaintsev, A. Vaivads, E. Georgescu, and R. Torbert, J. Geophys. Res. **13**, A12213, doi:10.1029/2008JA013385 (2008).
[7] L-.J. Chen, N. Bessho, B. Lefebvre, H. Vaith, A. Asnes, O. Santolik, A. Fazakerley, P. Puhl-Quinn, A. Bhattacharjee, Y. Khotyaintsev, P. Daly, and R. Torbert, Phys. Plasmas **16**, 056501 (2009)
[8] L-J. Chen, W. S. Daughton, B. Lefebvre, and R. B. Torbert, Phys. Plasmas **18**, 012904 (2011).
[9] L.-J., Chen, W. Daughton, A. Bhattacharjee, R. B. Torbert, V. Roytershteyn, and N. Bessho, Phys. Plasmas **19**, 112902 (2012).
[10] C. Z. Cheng, S. Inoue, Y. Ono, and R. Horiuchi, Phys. Plasmas **22**, 101205 (2015).
[11] W. Daughton, J. Scudder, and H. Karimabadi, Phys. Plasmas **13**, 072101 (2006).
[12] J. F. Drake, M. Swisdak, H. Che, and M. A. Shay, *Nature* **443**, 553 (2006).
[13] J. F. Drake, M. A. Shay, and M. Swisdak, Phys. Plasmas **15**, 042306 (2008).
[14] J. P. Eastwood, M. A. Shay, T. D. Phan, and M. Øieroset, Phys. Rev. Lett. **104**, 205001 (2010).
[15] J. Egedal, M. Øieroset, W. Fox, and R. P. Lin, Phys. Rev. Lett. **94**, 025006 (2005).
[16] J. Egedal, W. Fox, N. Katz, M. Porkolab, M. Øieroset, R. P. Lin, W. Daughton, and J. F. Drake, J. Geophys. Res. **113**, A12207, doi:10.1029/2008JA013520 (2008).
[17] K. Fujimoto, Phys. Plasmas **13**, 072904 (2006).
[18] K. Fujimoto and M. Takamoto, Phys. Plasmas **23**, 012903 (2016).
[19] K. J. Genestreti, S. A. Fuselier, J. Goldstein, T. Nagai, and J. P. Eastwood, J. Atmos. Sol.-Terr. Phys. **121**, 98 (2014).
[20] M. V. Goldman, D. Newman, and G. Lapenta, Space Science Reviews , 199, 651 (2016).
[21] C. C. Haggerty, M. A. Shay, C. T. McHugh, J. F. Drake, T. D. Phan, Geophys. Res. Lett. in press, doi:10.1002/2015GL065961 (2015).
[22] M. Hesse, K. Schindler, J. Birn, and M. Kuznetsova, Phys. Plasmas **6**, 1781 (1999).
[23] M. Hesse, S. Zenitani, and A. Klimas, Phys. Plasmas **15**, 112102 (2008).
[24] M. Hesse, T. Neukirch, K. Schindler, M. Kuznetsova, and S. Zenitani, *Space Sci. Rev.* **160**, 3, doi:10.1007/s11214-010-9740-1 (2011).
[25] H. Hietala, J. F. Drake, T. D. Phan, J. P. Eastwood, Geophys. Res. Lett. **42**, doi:10.1002/2015GL065168 (2015).
[26] R. Horiuchi and H. Ohtani, Commun. Comput. Phys. **4**, 496 (2008).
[27] M. Hoshino, T. Mukai, T. Terasawa, and I. Shinohara, J. Geophys. Res. **106**, 25979, doi:10.1029/2001JA900052 (2001).
[28] M. Hoshino, K. Hiraide, T. Mukai, *Earth, Planets and Space*, **53**, 627 (2001).
[29] J. Jara-Almonte, W. Daughton, H. Ji, Phys. Plasmas **21**, 032114 (2014).
[30] H. Karimabadi, W. Daughton, and J. Scudder, Geophys. Res. Lett. **34**, L13104, doi:10.1029/2007GL030306 (2007).
[31] A. Klimas, M. Hesse, and S. Zenitani, Phys. Plasmas **15**, 082102 (2008).
[32] A. Le, J. Egedal, W. Daughton, J. F. Drake, W. Fox, and N. Katz, Geophys. Res. Lett. **37**, L03106, doi:10.1029/2009GL041941 (2010).

[33]A. Le, J. Egedal, O. Ohia, W. Daughton, H. Karimabadi, and V. S. Lukin, Phys. Rev. Lett. **110**, 135004 (2013).
[34]A. Le, J. Egedal, J. Ng, H. Karimabadi, J. Scudder, V. Roytershteyn, W. Daughton, and Y.-H. Liu, Phys. Plasmas **21**, 012103 (2014).
[35]B. Li, R. Horiuchi, Phys. Rev. Lett. **101**, 215001 (2008).
[36]R.-F. Lottermoser, M. Scholer, and A. P. Matthews, J. Geophys. Res. **103**, 4547, doi:10.1029/97JA01872 (1998).
[37]T. Nagai, I. Shinohara, M. Fujimoto, A. Matsuoka, Y. Saito, and T. Mukai, J. Geophys. Res. **116**, A04222, doi:10.1029/2010JA016283 (2011).
[38]T. Nagai, S. Zenitani, I. Shinohara, R. Nakamura, M. Fujimoto, Y. Saito, and T. Mukai, J. Geophys. Res. **118**, 7703, doi:10.1002/2013JA019135 (2013).
[39]M. S. Nakamura, M. Fujimoto, and K. Maezawa, J. Geophys. Res. **103**, 4531, doi:10.1029/97JA01843 (1998).
[40]J. Ng, J. Egedal, A. Le, W. Daughton, and L.-J. Chen, Phys. Rev. Lett. **106**, 065002 (2011).
[41]M. Oka, T.-D. Phan, M. Øieroset, and V. Angelopoulos, J. Geophys. Res. **121**, 1955, doi:10.1002/2015JA022040 (2016).
[42]T. D. Phan, J. F. Drake, M. A. Shay, F. S. Mozer, and J. P. Eastwood, Phys. Rev. Lett. **99**, 255002 (2007).
[43]T. D. Phan, M. A. Shay, J. T. Gosling, M. Fujimoto, J. F. Drake, G. Paschmann, M. Oieroset, J. P. Eastwood, and V. Angelopoulos, Geophys. Res. Lett. **40**, 4475 (2013).
[44]P. L. Pritchett, J. Geophys. Res. **106**, 3783, doi:10.1029/1999JA001006 (2001).
[45]P. L. Pritchett, J. Geophys. Res. **106**, 25961, doi:10.1029/2001JA000016 (2001).
[46]P. L. Pritchett and F. V. Coroniti, J. Geophys. Res. **109**, A01220, doi:10.1029/2003JA009999 (2004).
[47]P. L. Pritchett, J. Geophys. Res. **110**, A05209, doi:10.1029/2004JA010948 (2005).
[48]P. L. Pritchett, J. Geophys. Res. **113**, A06210, doi:10.1029/2007JA012930 (2008).
[49]J. Scudder and W. Daughton, J. Geophys. Res. **113**, A06222, doi:10.1029/2008JA013035 (2008).
[50]M. A. Shay, J. F. Drake, and M. Swisdak, Phys. Rev. Lett. **99**, 155002 (2007).
[51]M. A. Shay, C. C. Haggerty, T. D. Phan, J. F. Drake, P. A. Cassak, P. Wu, M. Oieroset, M. Swisdak, and K. Malakit, Phys. Plasmas **21** 122902 (2014).
[52]J. R. Shuster, L.-J. Chen, W. S. Daughton, L. C. Lee, K. H. Lee, N. Bessho, R. B. Torbert, G. Li, and M. R. Argall, Geophys. Res. Lett. **41**, 5389, doi:10.1002/2014GL060608 (2014).
[53]J. R. Shuster, L.-J. Chen, M. Hesse, M. R. Argall, W. Daughton, R. B. Torbert, and N. Bessho, Geophys. Res. Lett. **42**, doi:10.1002/2015GL063601 (2015).
[54]B. U. Ö. Sonnerup, "Magnetic field reconnection," in *Solar System Plasma Physics*, edited by L. J. Lanzerotti, C. F. Kennel, and E. N. Parker (North-Holland, New York, 1979), Vol. 3, p.45.
[55]T. W. Speiser, J. Geophys. Res. **70**, 4219, doi:10.1029/JZ070i017p04219 (1965).
[56]M. Swisdak, J. F. Drake, M. A. Shay, J. G. McIlhargey, J. Geophys. Res. **110**, A05210 (2005).
[57]M. Swisdak, Geophys. Res. Lett. **43**, 43, doi:10.1002/2015GL066980 (2016).
[58]K. G. Tanaka, A. Retinò, Y. Asano, M. Fujimoto, I. Shinohara, A. Vaivads, Y. Khotyaintsev, M. André, M. B. Bavassano-Cattaneo, S. C. Buchert, and C. J. Owen, *Ann. Geophys.* **26**, 2471 (2008).
[59]S. Wang, L.-J. Chen, N. Bessho, L. M. Kistler, J. R. Shuster, and R. Guo, J. Geophys. Res. **121**, 2104, doi:10.1002/2015JA021892 (2016).
[60]Z.-D. Wang, J. Geophys. Res. **99**, 5949, doi:10.1029/93JA03174 (1994).
[61]X. Xu, Y. Wang, F. Wei, X. Feng, X. Deng, Y. Ma, M. Zhou, Y. Pang, and H.-C. Wong, *Scientific Reports* **5**, 8080, doi:10.1038/srep08080 (2015).
[62]S. Zenitani and M. Hoshino, Astrophys. J. , **562**, L63 (2001).
[63]S. Zenitani, M. Hesse, A. Klimas, and M. Kuznetsova, Phys. Rev. Lett. **106**, 195003 (2011).
[64]S. Zenitani, M. Hesse, A. Klimas, C. Black, and M. Kuznetsova, Phys. Plasmas **18**, 122108 (2011); e-print arXiv:1110.3103.
[65]S. Zenitani, I. Shinohara, and T. Nagai, Geophys. Res. Lett. **39**, L11102 (2012).
[66]S. Zenitani, I. Shinohara, T. Nagai, and T. Wada, Phys. Plasmas **20**, 092120 (2013).
[67]M. Zhou, X. H. Deng, Y. Pang, S. Y. Huang, Z. G. Yuan, H. M. Li, X. J. Xu, Y. H. Wang, M. Yao, D. D. Wang, Phys. Plasmas **19**, 072907 (2012).
[68]M. Zhou, X. Deng, B. Tang, Y. Pang, X. Xu, Z. Yuan, and S. Huang, J. Geophys. Res. **119**, 1541, doi:10.1002/2013JA019556. (2014).